Mitochondrial fusion dynamics is robust in the heart and depends on calcium oscillations and contractile activity

Verónica Eisner[a,b,1,2], Ryan R. Cupo[a,1], Erhe Gao[c], György Csordás[a], William S. Slovinsky[a], Melanie Paillard[a], Lan Cheng[a], Jessica Ibetti[c], S. R. Wayne Chen[d], J. Kurt Chuprun[c], Jan B. Hoek[a], Walter J. Koch[c], and György Hajnóczky[a,2]

[a]MitoCare Center, Department of Pathology, Anatomy, and Cell Biology, Thomas Jefferson University, Philadelphia, PA 19107; [b]Departamento de Biología Celular y Molecular, Facultad de Ciencias Biológicas, Pontificia Universidad Católica de Chile, Santiago 8330025, Chile; [c]Center for Translational Medicine, Temple University School of Medicine, Philadelphia, PA 19140; and [d]Department of Physiology and Pharmacology, University of Calgary, Calgary, AB, Canada, T2N 4N1

Edited by Eric N. Olson, University of Texas Southwestern Medical Center, Dallas, TX, and approved November 22, 2016 (received for review October 24, 2016)

Mitochondrial fusion is thought to be important for supporting cardiac contractility, but is hardly detectable in cultured cardiomyocytes and is difficult to directly evaluate in the heart. We overcame this obstacle through in vivo adenoviral transduction with matrix-targeted photoactivatable GFP and confocal microscopy. Imaging in whole rat hearts indicated mitochondrial network formation and fusion activity in ventricular cardiomyocytes. Promptly after isolation, cardiomyocytes showed extensive mitochondrial connectivity and fusion, which decayed in culture (at 24–48 h). Fusion manifested both as rapid content mixing events between adjacent organelles and slower events between both neighboring and distant mitochondria. Loss of fusion in culture likely results from the decline in calcium oscillations/contractile activity and mitofusin 1 (Mfn1), because (*i*) verapamil suppressed both contraction and mitochondrial fusion, (*ii*) after spontaneous contraction or short-term field stimulation fusion activity increased in cardiomyocytes, and (*iii*) ryanodine receptor-2–mediated calcium oscillations increased fusion activity in HEK293 cells and complementing changes occurred in Mfn1. Weakened cardiac contractility in vivo in alcoholic animals is also associated with depressed mitochondrial fusion. Thus, attenuated mitochondrial fusion might contribute to the pathogenesis of cardiomyopathy.

mitochondria | fusion | calcium | alcohol | cardiomyopathy

Cardiac contractions require a constant energy supply, which is provided by mitochondrial metabolism. ATP is needed for excitation-contraction coupling (ECC) for both contraction and relaxation in each cycle (1, 2). ECC-associated cytoplasmic Ca^{2+} transients ($[Ca^{2+}]_c$) are propagated to the mitochondrial matrix (3) to regulate Ca^{2+}-dependent mitochondrial dehydrogenases, ATP synthesis, and intracellular Ca^{2+} homeostasis (4). Thus, cardiac mitochondria are forced to work permanently and likely require quality control mechanisms to keep them in a functioning state.

In many tissues, mitochondria are permanently rebuilt through evolutionarily conserved cyclic processes of fusion and fission. Fusion involves content exchange, allowing complementation of mitochondrial solutes, proteins, and DNA. Fission allows segregation of damaged components (5, 6). Both fusion and fission are promoted by mitochondrial movements that can bring distant mitochondria close to one another and can also separate interacting structures (7). However, the spatial arrangements and mitochondrial morphology are determined by sarcomers in ventricular myocytes, the contractile units of the adult mammalian heart. The gaps among densely packed parallel myofibrils are inhabited by bullet-like mitochondria that run longitudinally, interacting intimately with the junctional sarcoplasmic reticulum (SR), in a conformation that facilitates Ca^{2+} exchange and supports ECC (4, 8). Despite the spatial restrictions intrinsic to adult cardiomyocyte mitochondria, interactions among these organelles have been proposed based on functional observations. Reactive oxygen species (ROS)-induced ROS release (9, 10) and so-called "energy-transmitting cables" (11) suggest the presence of intermitochondrial signaling. Recent data describing intermitochondrial junctions and spatially organized cristae arrays indicate that physical structures support the communication among cardiac mitochondria (12). Reports on genetic targeting of mitochondrial fusion or fission in cardiac-derived cell lines (13) and neonatal cardiomyocytes (14), as well as regulation of mitochondrial fission by $[Ca^{2+}]_c$ transients in neonatal cardiomyocytes (15), suggest that mitochondrial dynamics might be an active process in the heart; however, there are no published studies like these in fully differentiated adult ventricular myocytes (AVCMs).

In cultured AVCMs, low-frequency mitochondrial matrix content exchange has been shown, largely mediated by stable connecting structures known as nanotunnels (16). In adult skeletal muscle fibers, the other form of striated muscle, we (17) and others (18–20) have recently demonstrated that mitochondria are dynamically connected and undergo frequent fusion events dependent on an outer mitochondrial membrane (OMM) fusion protein, mitofusin 1 (Mfn1), and the inner mitochondrial membrane

Significance

Mitochondrial function is supported by dynamic quality control processes, such as mitochondrial fusion. Cardiac contractility depends on mitochondrial metabolism, yet in cardiomyocytes, mitochondria are confined among myofibrils, raising questions about the possibility of mitochondrial physical communication. Here we demonstrate that mitochondrial continuity is robust and fusion is frequent in freshly isolated rat ventricular myocytes, manifesting both as rapid content mixing events between adjacent organelles and slower, often long-distance events. We show that mitochondrial fusion decreases dramatically in culture because of the decay in contractile activity and, more specifically, the underlying calcium oscillations, which involve mitofusin 1 (Mfn1) abundance. In addition, we show that attenuation of cardiac contractility in vivo in alcoholic animals is also associated with depressed mitochondrial fusion.

Author contributions: V.E., R.R.C., G.C., J.B.H., W.J.K., and G.H. designed research; V.E., R.R.C., E.G., G.C., W.S.S., M.P., L.C., J.I., and J.K.C. performed research; S.R.W.C. contributed new reagents/analytic tools; V.E., R.R.C., G.C., and W.S.S. analyzed data; and V.E. and G.H. wrote the paper.

The authors declare no conflict of interest.

This article is a PNAS Direct Submission.

[1]V.E. and R.R.C. contributed equally to this work.

[2]To whom correspondence may be addressed. Email: veisner@bio.puc.cl or Gyorgy.Hajnoczky@jefferson.edu.

This article contains supporting information online at www.pnas.org/lookup/suppl/doi:10.1073/pnas.1617288114/-/DCSupplemental.

(IMM) fusion protein, Opa1 (17). In addition, recent studies have suggested that skeletal muscle reticular mitochondria support membrane potential propagation (19). In the heart, interference with such fusion proteins causes massive damage. Cardiac-specific ablation of Mfn1 and Mfn2 leads to mitochondrial fragmentation, impaired oxidative metabolism, and dilated cardiomyopathy (21) and compromises heart development (22). Moreover, targeting of Opa1 is detrimental to cardiac myocyte differentiation (22) and contractile function (23). In addition, imbalanced processing of Opa1 in the heart leads to mitochondrial fission and heart failure (24). Considering that mitochondrial fusion proteins in the heart have also been implicated in other functions, including cristae remodeling (25), SR–mitochondria communication (26), mitophagy (27), and apoptosis (28), the specific contribution of fusion to these cardiac impairments remains elusive.

Cardiac contractile activity and the corresponding energy needs fluctuate continually. In skeletal muscle, scanning electron microscopy has shown that acute exercise results in increased structural interactions among mitochondria (29). In addition, elevated Mfn1 and Mfn2 mRNA levels (30), as well as increased mitochondrial continuity (20), have been observed after exercise. Finally, slow-twitch/oxidative fibers that are permanently stimulated by action potentials exhibit a higher frequency of fusion events than fast-twitch/glycolytic fibers that exhibit isolated acute trains of stimulation (20, 31). Thus, it is plausible that cardiac contractile activity might exert some control over cardiac mitochondrial fusion. We speculate that the low frequency of mitochondrial fusion events previously documented in adult cardiomyocytes kept in culture for 48–72 h (16) might be a consequence of the decay in contractile and/or metabolic activity.

Contractile activity becomes depressed in dilated cardiomyopathy, a common cause of which is chronic alcohol consumption (32). Mitochondria are a primary target of alcoholic tissue injury (33), and altered mitochondrial ultrastructure has been reported in alcoholic cardiac cells (34). In addition, our previous studies documented attenuated mitochondrial fusion dynamics in both skeletal muscle fibers (17) and hepatocytes (35) isolated from ethanol (EtOH)-fed rats. To investigate whether suppressed mitochondrial quality control might be a factor in the progression of alcoholic cardiac muscle dysfunction, in the present work we evaluated cardiac mitochondrial dynamics in chronically EtOH-fed rats.

The technical challenges of measuring mitochondrial dynamics and the scanty information available on mitochondrial content exchange in contracting cardiomyocytes have precluded answering fundamental questions about mitochondrial quality control in the heart, including the specific mechanisms of content exchange, the dependence of content exchange events on ECC activity and the possible involvement of content exchange processes in cardiac disease. Here we applied photoactivatable fluorescent protein techniques to evaluate mitochondrial dynamics in cardiomyocytes and in intact heart.

Results

Matrix Continuity Among Mitochondria in Rat Cardiac Myocytes: Effect of Maturation State and Cell Culture. To study the interactions among mitochondria in cardiac myocytes, we expressed two mitochondrial matrix-targeted soluble fluorescent proteins, mtDsRed and mtPA-GFP, and evaluated their distribution by confocal microscopy. We selected between three and five 25-μm^2 square areas in each cell and illuminated them to achieve two-photon (2P) photoactivation (PA) of PA-GFP, and followed the spreading of mtPA-GFP out of the illuminated regions. The fluorescence decay within the PA areas represents the sum of diffusion within the mitochondrial network, mitochondrial fusion, and mitochondrial movement (17). Following the strategy described in a recent study (16), we first evaluated 24- to 48-h–cultured neonatal ventricular cardiomyocytes (NVCMs). NVCMs showed robust spreading of mtPA-GFP (Fig. 1 *A* and *B*, column 1 and Movie S1), reaching distant organelles within 5 min (quantified in Fig. 1*C*).

In contrast to mitochondria in NVCMs, mitochondria in AVCMs rearranged into longitudinal columns of apparently unconnected organelles and subgroups of less well-organized perinuclear organelles (Fig. 1 *A* and *B*, columns 2–4 and Fig. S1). AVCMs were first transformed in vitro by adenoviral mtDsRed and mtPA-GFP. Cells were infected promptly after plating and imaged 24–36 h later, once the fluorescent protein expression reached detectable levels. We focused on the interactions among intermyofibrillar mitochondria, given their role in regulating contractile function and their strategic orientation toward the SR (4). Spreading of mtPA-GFP beyond the edges of the PA area (Fig. 1 *A–C*, column 2 and Movie S2) demonstrated some continuity

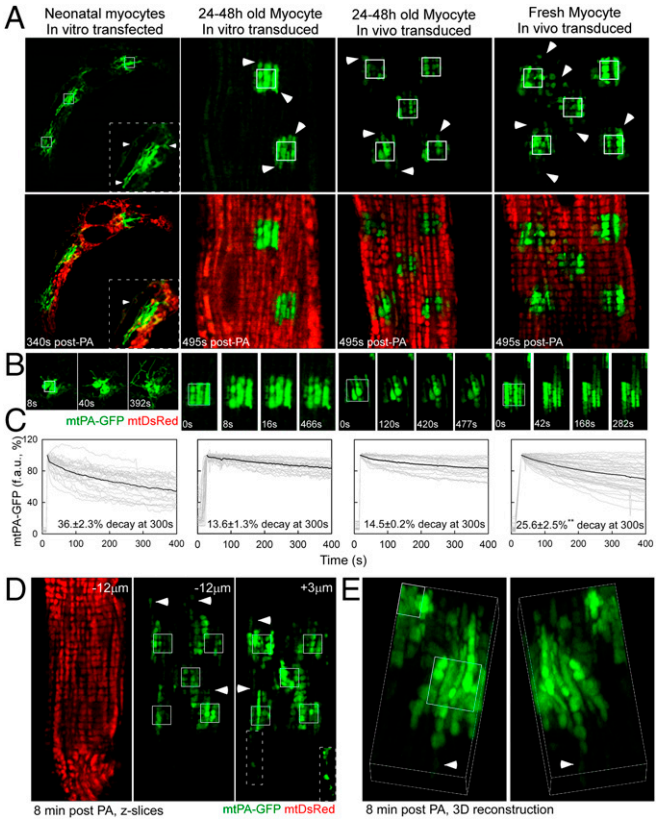

Fig. 1. Mitochondrial matrix continuity in cardiac myocytes. (*A*) Representative images of myocytes after 2P PA of mtPA-GFP (white outlined squares). Arrowheads indicate mtPA-GFP beyond the PA regions. mtDsRed reveals the whole mitochondrial population of in vitro-transfected NVCMs (column 1) and 24–48 h in vitro-cultured (column 2) or in vivo-transduced (column 3) and freshly isolated in vivo-transduced (column 4) AVCMs. (*B*) Time series of one PA region for each condition. (*C*) mtPA-GFP fluorescence decay kinetics in a PA region in in vitro-transfected NVCMs ($n = 20$) and AVCMs ($n = 30$) and in vivo-transduced and cultured ($n = 20$) and freshly isolated AVCMs ($n = 47$). Gray curves denote individual regions; black curves represent the mean. $P < 0.01$. (*D*) Mitochondrial distribution in a freshly isolated AVCM (*Left*), and the diffusion of mtPA-GFP at −12 μm below (*Center*) and +3 μm above (*Right*) the 2P illuminated focal plane. (*Inset*) The spread of mtPA-GFP along a continuous chain of connected mitochondria. Arrows highlight organelles located distant from the PA regions. (*E*) A 3D reconstruction of a freshly isolated myocyte. The arrowhead indicates a distant organelle containing mtPA-GFP.

among mitochondria in AVCMs; however, this diffusion was limited and only over short distances.

We reasoned that because culture conditions negatively affect contractile function (36), they also might alter mitochondrial dynamics. Thus, our next step was to perform in vivo adenoviral infection of the ventricular walls of adult rat hearts. Then, 7–10 d later, we isolated AVCMs and plated them for microscopic evaluation at 24–48 h postharvest or promptly after plating. Fig. 1 *A*–*C*, column 3 and Movie S3 show diffusion of mtPA-GFP comparable to that observed in in vitro-transformed AVCMs (column 2). Freshly isolated in vivo-transduced AVCMs exhibited significant mitochondrial continuity, characterized by both longitudinal and transversal diffusion of mtPA-GFP (Fig. 1*A*, column 4 and Movies S4 and S5), extending >5 μm away from the PA region (Fig. 1*B*). We also found a significant decrease in mtPA-GFP fluorescence within the PA regions, with 25.6% decay at 300 s, as opposed to 14.5% in cultured AVCMs ($P < 0.01$) (Fig. 1*C*).

We further evaluated the diffusion of mtPA-GFP above and below the PA focal plane in fresh AVCMs by means of Z-stack imaging at 8 min after PA. Mitochondria containing photoactivated mtPA-GFP were found even 12 μm below (−12 μm) the PA focal plane (Fig. 1*D*). In addition, at the +3 μm focal plane, a discrete row of mitochondria projected toward the periphery, extending 12 μm away from the PA region. Finally, high-magnification 3D projections from a different cell (Fig. 1*E*) showed mitochondrial matrix continuity in both longitudinal and transversal orientations in a freshly isolated AVCM. We performed a comparable 3D analysis in in vitro- and in vivo-transduced, AVCMs cultured for 24–48 h and found a drastic decrease in mitochondrial continuity compared with freshly isolated myocytes (Fig. S1*B*). We conclude that mitochondria in AVCMs form complex networks with matrix content exchange, and that culture conditions cause suppression of mitochondrial communication. Moreover, in NVCMs, mitochondria are less ordered and communicate actively with their neighbors.

Active Mitochondrial Fusion Dynamics in Freshly Isolated AVCMs. We next evaluated the mitochondrial fusion activity in freshly isolated AVCMs transduced with the reporters in vivo. When mtPA-GFP is photoactivated, mtDsRed becomes photobleached in the same area, producing green-only mitochondria surrounded by red-only mitochondria. During the merging of green-only and red-only mitochondria, abrupt complementary changes in green and red fluorescence validate fusion pore opening and matrix content mixing driven by the concentration gradient. We observed fusion events among intermyofibrillar mitochondria, showing diverse orientations and kinetics (Fig. 2 *A* and *B*). Images of an AVCM before and 12 s after PA highlight the early spreading of PA-GFP (Fig. 2*A*), which indicates preexisting matrix continuity among individual mitochondria. Further examination of the distribution of mtPA-GFP in discrete mitochondria located in the proximity of the PA areas revealed abrupt increases in the area of the fluorescent protein, corresponding to mitochondrial fusion events; as an example, a series of organelles underwent sequential fusion events in longitudinal orientation (Fig. 2*B*). Another example shows a subregion of a PA area and its surroundings, presenting four sequential fusion events in both longitudinal and transversal orientations, characterized by a decrease in PA-GFP fluorescence in the donor mitochondrion and a parallel increase in a nearby acceptor mitochondrion (Fig. S2*A* and Movie S6). Noticeably, NVCMs also exhibited sequential fusion events among neighboring mitochondria (Fig. S2*B*). In quantitative analyses of the fusion events in AVCMs maintained under different culture conditions (Fig. S2*C*), freshly isolated AVCMs exhibited 1.4 ± 0.1 events/min, whereas cultured in vivo-transduced AVCMs showed four-fold fewer events, and cultured in vitro-transformed AVCMs showed

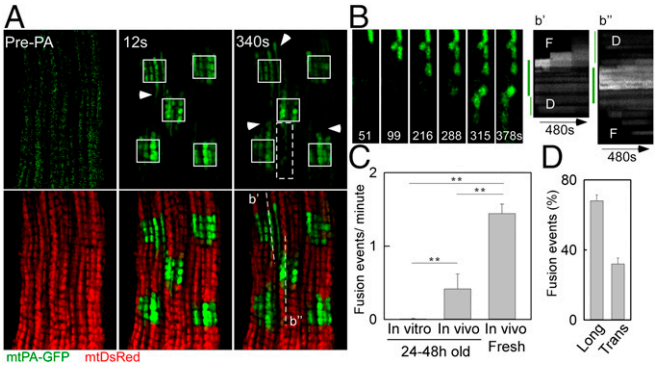

Fig. 2. Mitochondrial fusion in freshly isolated AVCMs. (*A*) A representative AVCM before and after 2P PA of mtPA-GFP (white squares). At 12 s, the spreading of mtPA-GFP fluorescence indicates matrix continuity among mitochondria (arrowhead). At 340 s, newly formed communication (arrowheads) is observed. (*B*, *Left*) mtPA-GFP time series for the area marked by the white-dashed box in *A*, denoting serial fusion events in a longitudinal orientation. (*B*, *Right*) Here b′ and b′′ represent a line-scan analysis of the indicated dashed lines in *A*. The thick green line indicates the PA area. D, initial diffusion of mtPA-GFP toward the vicinity of the PA region, also denoted by the thin green line on the left. F, step-like mtPA-GFP fluorescence transfer corresponding to fusion event. (*C*) Fusion frequency in cultured and freshly isolated AVCMs (in vitro-transformed AVCMs cultured for 24–48 h: 26 cells, seven experiments; in vivo-transformed AVCMs cultured for 24 h: nine cells, two experiments; in vivo-transformed freshly isolated AVCMs: 34 cells, four experiments). $^{**}P < 0.01$. (*D*) Frequency of longitudinal (Long) and transverse (Trans) fusion events.

almost no events (a rare event is shown in Fig. S2*C*). Thus, AVCM mitochondria regularly undergo fusion, and this activity decays in culture.

Transmission electron microscopy (TEM) in fixed heart muscles has demonstrated that intermyofibrillar mitochondria run parallel to myofibrils, mostly forming columns of individual mitochondria, accompanied by some transversally oriented organelles. Such a distribution in live AVCMs is also supported by our confocal microscopy data. Moreover, the fusion events occurred predominantly among longitudinally oriented organelles (Fig. 2*D*), although 32% of the interactions occurred transversally.

Slow Matrix Content Mixing Events in AVCMs. Different from other cells that we have studied previously, including mouse embryonic fibroblasts (MEFs), H9c2 cells, hepatocytes, and skeletal muscle fiber cells (7, 17, 35), AVCMs exhibited diverse mixing kinetics of the matrix-targeted fluorescent proteins (Fig. 3). Two representative examples are shown in Fig. 3*A* and Movie S7. In the figure, the left panel shows an event with fast mixing kinetics between two longitudinally oriented mitochondria. This mixing event was completed within 12 s, as validated by the time course of both PA-GFP and DsRed in the donor and acceptor mitochondria. The complementary equilibration of both fluorescent proteins confirms that a fusion event occurred. The right panel shows a comparable fusion event example in terms of location relative to the PA region and size of both the PA-GFP donor and the acceptor. The transfer of the fluorescent proteins was slower, however, taking 70 s to reach equilibrium. The slow mixing kinetics applied to both fluorescent proteins, arguing against the possibility of an artifact associated with the conformation of either protein. Thus, based on the mixing kinetics, we discriminated between fast and slow fusion events, which are completed in <12 s and >12 s of mitochondrial matrix mixing, respectively. Overall, slow mixing kinetics fusion events are prevalent in AVCMs (Fig. 3*D*) and are likely to represent a tissue-specific feature of cardiac mitochondrial fusion.

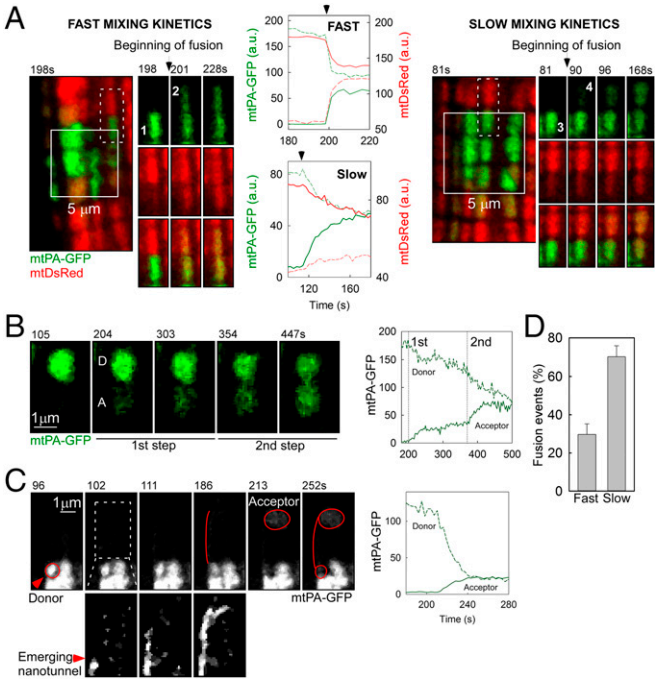

Fig. 3. Kinetics of fusion events in AVCMs. (*A*) Examples of fusion with fast (*Left*; mitochondria 1 and 2) and slow (*Right*; mitochondria 3 and 4) mixing kinetics. The locations of the involved organelles are indicated by white dashes. The time series shows the transfer of mtPA-GFP (photoactivated within the PA area) and mtDsRed (photobleached at the same time) in opposite directions. Central plots represent the quantification of mtPA-GFP and mtDsRed exchange. (*B*) A slow mixing kinetics fusion event displaying a two-step mixing kinetics, between donor (D) and acceptor (A) mitochondria. (*Left*) Representative image series. (*Right*) Quantitative plot. (*C*) A slow mixing kinetics fusion event between two distant mitochondria (D and A) connected by a narrow mitochondrial structure, from D to A. (*Bottom Left*) The dashed rectangle with enhanced brightness highlighting an emerging nanotunnel-like structure. (*Right*) Slow mixing kinetics leading to equilibration of fluorescence. (*D*) Frequency of fast and slow events (n = 51 cells).

We next searched for possible explanations for the slow matrix mixing kinetics. We found some evidence suggesting the IMM fusion pore might open in an intermittent fashion (Fig. 3*B* shows a two-step fusion event), similar to the fusion between exocytotic vesicles and the plasma membrane (37). Overall, 11% of the slow mixing kinetics events displayed detectable multistep mixing kinetics (Fig. S3*A* and Movie S8). Furthermore, the previously described narrow intermitochondrial nanotunnels (16) also might support slow content mixing. Indeed, we observed a nanotunnel-like structure growing out from a small PA-GFP–carrying mitochondrion and reaching a distant mitochondrion, which was associated with slow mixing kinetics (Fig. 3*C*). We also detected slow mixing kinetics between two non-neighbor mitochondria (Fig. S3*A*). In addition, we found narrow tubules apparently emerging from larger mitochondria (Fig. S3*B* and Movie S9). These examples demonstrate a fluorescence distribution consistent with the presence of nanotunnels, and demonstrate that these structures make mitochondrial soluble content exchange possible, accompanied by slow mixing kinetics.

Mitochondrial Fusion Dynamics in Whole Heart. To image mitochondria in intact tissue, in vivo-infected whole hearts were perfused and examined by confocal microscopy. The mitochondrial structure in the outer layer of myocytes in the ventricular wall was first visualized using tetramethylrhodamine, ethyl ester (TMRE), which accumulates in the mitochondria in a membrane potential-dependent manner (Fig. 4*A*). Cardiomyocytes of the ventricular wall of in vivo-transformed hearts exhibited mtDsRed fluorescence distribution comparable to TMRE localization (Fig. 4*B*). Approximately 40% of the myocytes expressed mtDsRed. Once we found a myocyte positioned parallel to the coverslip and showing well-defined organelles, we applied 2P illumination in discrete 25-µm^2 square regions and followed the time course after the PA of mtPA-GFP. Immediately after the end of PA, mtPA-GFP diffused into the surrounding mitochondria around the PA regions, mostly in longitudinal orientations (Fig. 4*C*, *Inset*, R1). Interestingly, at 6 min after PA, region 4 showed a new mitochondrion located 1 µm away from the corner of R4 and transversally oriented to the PA-GFP–containing mitochondria inside it, possibly indicating a fusion event. Owing to contraction, recording the kinetics of PA-GFP spreading was difficult; nonetheless, some decay in PA-GFP fluorescence was apparent even in the first 80 s after PA (Fig. 4*D*). Despite the complexity of the recording, we could identify fusion events. One example shows the mixing of mtPA-GFP and mtDsRed between two neighbor mitochondria (Fig. 4*E*). Therefore, these data confirm that the observed mitochondrial fusion activity found in isolated myocytes also occurs within cardiac muscle.

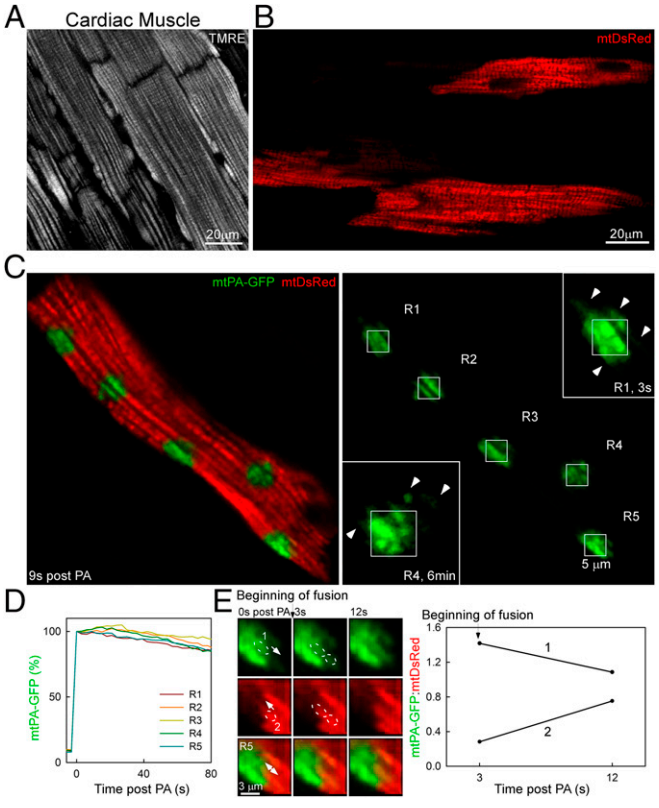

Fig. 4. Mitochondrial continuity and fusion events in the whole heart. (*A*) Ventricular myocytes in the outer layer of the ventricular wall of a TMRE-perfused whole heart. (*B*) Ventricular myocytes from an in vivo-transformed whole heart showing mtDsRed fluorescence. (*C*) A ventricular myocyte in the whole heart. Right side mtPA-GFP image denotes five PA regions (R1–5). R1 and R4 were zoomed in at 3 s and 6 min, respectively. (*D*) Plot showing the mtPA-GFP decay kinetics in the PA area. (*E*) Images of a time series of a fusion event between two adjacent mitochondria, 1 and 2. The plot shows the opposite fluorescence transfer as the mtPA-GFP/mtDsRed ratio for each organelle.

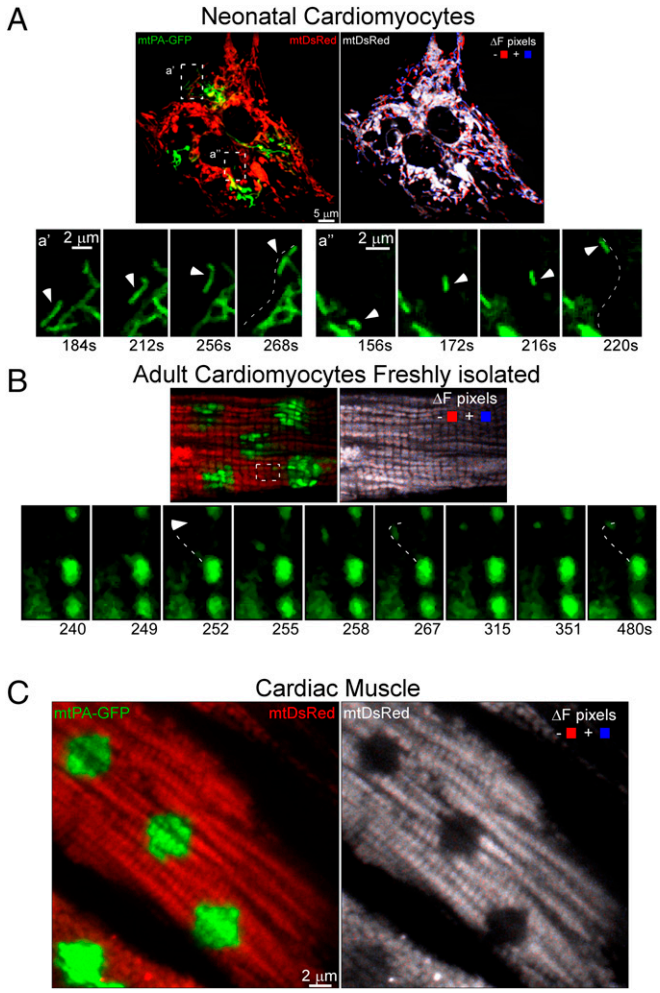

Fig. 5. Mitochondrial motility in heart cells. (*A*) NVCMs. (*Left*) In the green and red image acquired at 184 s post-PA of mtPA-GFP, the white boxes labeled a′ and a′′ show regions in which isolated mitochondrial displacements are apparent. (*Bottom*) Time series illustrating the movement of a single mitochondrion in the a′ and a′′ regions. The trajectory of each organelle is indicated by a white-dashed line. (*Right*) Processed image shows both mtDsRed fluorescence (grayscale) and the sites of mitochondrial movement calculated by subtraction of F(mtDsRed) at 4 s from F(mtDsRed) at 16 s. Red indicates negative changes; blue, positive changes. (*B*, *Upper Left*) In vivo-transformed AVCMs at 180 s post-PA of mtPA-GFP shows minimal displacement of individual mitochondria. (*B*, *Right*) There were few moving mitochondria, as indicated by the low number of ΔF pixels. The dashed lines show one mitochondrion moving toward the upper side of the cell. (*B*, *Bottom*) A detailed view of the trajectory of this directional movement. (*C*) Mitochondrial movement in an AVCM in the whole heart at 20 s after PA.

Motility of Mitochondria in Cardiac Myocytes. Given the relevance of mitochondrial movements as a facilitator of mitochondrial encounters and fusion events (7, 38), we studied motility in ventricular myocytes. NVCMs exhibited highly active mitochondrial movements throughout the cells (Fig. 5*A*). In contrast, cultured AVCMs showed minimal motility (data not shown). Moreover, mitochondria in the whole heart did not exhibit motility (Fig. 5*C*); however, some motility activity was present in freshly isolated AVCMs (Fig. 5*B*). In addition to Brownian-like movements (Fig. 5*B*), we found an isolated displacement motility event restricted to a small region (Fig. 5*B*, *Lower*). The limited motility observed in the AVCMs indicates that mitochondrial movements do not have a major role in supporting mitochondrial fusion in cardiac muscle.

Mitochondrial Fusion Depends on Excitation-Contraction Activity. The forgoing results indicate a negative effect of cell culture conditions on mitochondrial communication in AVCMs. The regular ECC activity decays in AVCMs after isolation and culture. This raises the possibility that ECC function is required to support mitochondrial fusion, which we tested more directly using the following approach. We first treated the cells with verapamil, an inhibitor of Ca^{2+} entry via L-type Ca^{2+} channels to suppress contractile activity in neonatal and freshly isolated ventricular myocytes. This treatment caused fewer cells to contract and contracting cells to show fewer contractions (Fig. 6 *A* and *B*, *Left*), and partially decreased the mitochondrial fusion event rate in both NVCMs and freshly isolated AVCMs (Fig. 6 *A* and *B*, *Right*). We also analyzed the rate of fusion events before and after the occurrence of a spontaneous contraction in AVCMs, and detected an increase in mitochondrial fusion frequency in the first 2 min after a spontaneous contraction (Fig. 6*C*). Finally, we evaluated the short-term effect of ECC activity

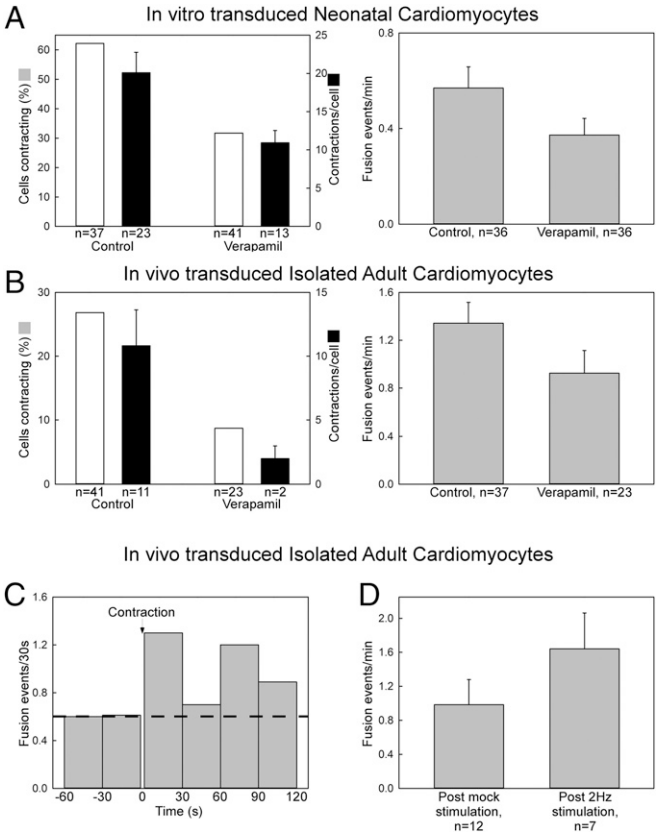

Fig. 6. Effect of contractile activity on mitochondrial fusion dynamics. (*A*) NVCMs transfected with mtDsRed and mtPA-GFP were treated with verapamil 10 μM for 48 h, followed by confocal microscopy evaluation. (*Left*) Bar chart showing the percentage of contracting cells (white) and the number of contractions per cell (black). (*Right*) Mitochondrial fusion event frequency. (*B*) Freshly isolated in vivo-transduced AVCMs were treated with verapamil 10 μM for at least 4 h and no longer than 6 h. (*Left*) Bar chart showing the percentage of contracting cells (white) and the number of contractions per cell (black). (*Right*) Fusion event frequency. (*C*) Temporal distribution of fusion events relative to a spontaneous contraction in non-stimulated in vivo-transduced freshly isolated AVCMs. The cells did not show spontaneous contraction in the minutes before the contraction evaluated (n = 10 cells). (*D*) Freshly isolated in vivo-transduced AVCMs expressing mtDsRed that responded by contraction to isolated electric pulses were field-stimulated (5 min) without 2,3-butanedione monoxime (BDM) during confocal microscopy and then evaluated for fusion events in 10 mM BDM-supplemented 0.25% BSA extracellular medium (ECM).

in freshly isolated AVCMs by field-stimulating the cells for 5 min. (Fig. S4 shows a schematic presentation of the stimulation protocol.) After stimulation, we found a 60% increase in mitochondrial fusion compared with control cells (Fig. 6*D*). Thus, we conclude that regular ECC facilitates the mitochondrial fusion activity of AVCMs.

RyR2-Mediated $[Ca^{2+}]_c$ Oscillations Are Sufficient to Promote Mitochondrial Fusion. Each ECC event in AVCMs is triggered by plasma membrane depolarization and an ensuing $[Ca^{2+}]_c$ transient. To isolate the potential role of the depolarization and $[Ca^{2+}]_c$ increase from contraction, we first used noncontracting H9c2 cardiac myoblasts. Depolarization evoked by increased KCl and $[Ca^{2+}]_c$ elicited by a Ca^{2+} ionophore, ionomycin, failed to induce an increase in mitochondrial connectivity (Fig. 7 *A* and *B*). However, ionomycin causes a single and prolonged $[Ca^{2+}]_c$ rise, whereas AVCMs display RyR2-mediated $[Ca^{2+}]_c$ oscillations. A surrogate for these $[Ca^{2+}]_c$ oscillations without contractile activity is provided by HEK293 cells expressing RyR2 (HEK-RyR2) in a tetracycline-inducible manner (39). Indeed, tetracycline-pretreated HEK-RyR2 cells displayed a moderately elevated average $[Ca^{2+}]_c$ compared with nontreated cells (Fig. 7*C*), owing to an increase in the fraction of cells with $[Ca^{2+}]_c$ spiking from 4.6% to 63.6%, manifesting in the form of baseline–spike $[Ca^{2+}]_c$ oscillations (Fig. 7*D*). Simultaneous imaging of $[Ca^{2+}]_c$ and mitochondrial dynamics (with mtDsRed and mtPA-GFP) revealed no difference in mitochondrial morphology between nonoscillating and oscillating HEK-RyR2 cells (Fig. 7 *E* and *F*); however, the spread of the matrix-targeted fluorescent proteins, and specifically the number of mitochondrial fusion events, was enhanced in the oscillating cells (Fig. 7*G*). Interestingly, when caffeine (10 mM), a stimulator of RyR2, was added, a single and large $[Ca^{2+}]_c$ transient occurred, and the oscillations stopped (Fig. 7*H*). This was followed by decreases in mitochondrial matrix continuity and fusion activity (Fig. 7*I*). Taken together, these results suggest that the effect of cardiac contractile activity on mitochondrial fusion could be mediated by the $[Ca^{2+}]_c$ oscillations.

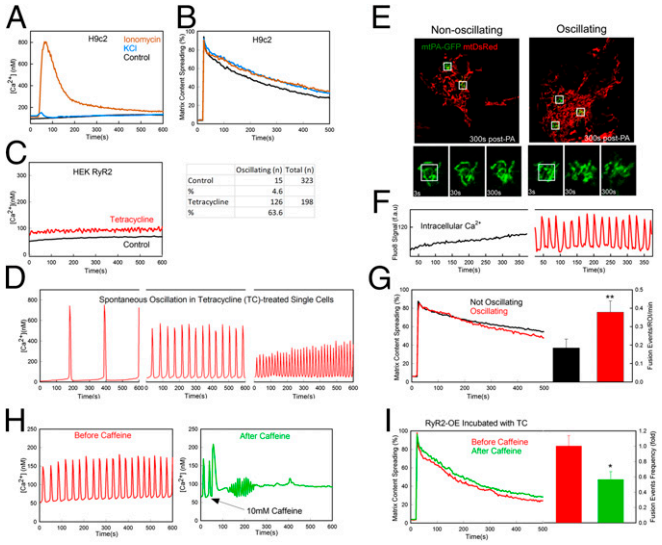

Fig. 7. Effect of calcium oscillations and plasma membrane depolarization on mitochondrial dynamics in H9c2 and HEK cells. (*A*) Fura2-AM–loaded H9c2 cells were treated with 60 mM KCl (n = 179), treated with 5 μM ionomycin (n = 159), or left untreated (control; n = 348) at 30 s. $[Ca^{2+}]_c$ was recorded every 3 s for 10 min. (*B*) The change in mtPA-GFP/mtDsRed is shown for H9c2 cells treated with 60 mM KCl (n = 31), treated with 5 μM ionomycin (n = 27), or untreated from 5 min before imaging (n = 36 cells). (*C*, *Left*) HEK-RyR2 cells induced with tetracycline show increased mean basal $[Ca^{2+}]_c$ compared with WT because of spontaneous oscillations. (*C*, *Right*) Percentage of cells in each group showing spontaneous oscillation. (*D*) Samples of HEK-RyR2 cells showing spontaneous calcium oscillation measured with Fluo8-AM show greater amplitude when the oscillations occur at a lower frequency. (*E*) Spreading of mtPA-GFP and recovery of mtDsRed in nonoscillating and oscillating HEK-RyR2 cells (*Upper*) and time series of one PA region from the cells in the upper panel (*Lower*). (*F*) $[Ca^{2+}]_c$ recorded with Fluo8 (fluorescence arbitrary units) in the cells shown in *E*. (*G*) Comparison of mtPA-GFP spreading between oscillating and nonoscillating HEK-RyR2 cells. Mean spreading rates show little difference (*Left*); however, the oscillating cells (n = 30) show roughly a twofold increase in fusion events per PA region compared with the nonoscillating cells (n = 34) (*Right*). $^{**}P < 0.01$. (*H*) $[Ca^{2+}]_c$ in a single oscillating HEK-RyR2 cell before and after treatment with 10 mM caffeine (n = 314 and 297, respectively). (*I*) Comparison of GFP diffusion and relative rates of fusion frequency in HEK-RyR2 cells before and after caffeine treatment (n = 12 and 13, respectively, for PA-GFP diffusion; n = 6 and 7, respectively, for mitochondrial fusion; $P < 0.05$).

To identify the potential target of ECC activity/$[Ca^{2+}]_c$ oscillations in the control of mitochondrial fusion, we quantified the abundance of OMM and IMM fusion proteins in freshly isolated and overnight-cultured AVCMs. Immunoblotting indicated significantly decreased Mfn1 in the overnight-cultured AVCMs, but no change in Mfn2 and Opa1 (Fig. S5*A*). To test for a cause-and-effect relationship between Mfn1 decrease and decay in mitochondrial fusion activity, we used an adenovirus carrying a mouse Mfn1 expression construct (which shares 99% homology with rat Mfn1) to in vitro-transform freshly isolated AVCMs in vivo-infected with AdmtDsRed and AdmtPA-GFP. The cells were kept in culture for 24–48 h before mitochondrial fusion was tested. We found that exogenous expression of Mfn1 in the cultured AVCMs rescued mitochondrial continuity and fusion frequency compared with cells transformed with a control adenovirus, AdLacZ (Fig. S5*C*). The efficiency of AdMfn1 for actually rescuing the expression of Mfn1 was validated in MEF $Mfn1^{-/-}$ cells in terms of both Mfn1 abundance and mitochondrial morphology (Fig. S5*B*). Complementing the results in AVCMs, HEK-RyR2 cells displayed higher Mfn1 levels compared with plain HEK cells (Fig. S5*D*). Thus, these results indicate that ECC activity/RyR2-mediated $[Ca^{2+}]_c$ oscillations help maintain Mfn1 abundance as a mechanism to support mitochondrial fusion activity. A decrease in Mfn1 might account for the long-term effects of ECC activity, but is unlikely to explain the short-term changes in fusion activity observed on pacing in cultured AVCMs (Fig. 6*D*) and cessation of $[Ca^{2+}]_c$ oscillations in HEK-RyR2 cells (Fig. 7*I* and *Discussion*).

Suppression of Cardiac Mitochondrial Fusion by Chronic EtOH Exposure. Environmental and dietary stressors target the heart's contractile performance and represent a leading cause of death worldwide. Among these stressors, chronic EtOH consumption leads to dilated cardiomyopathy (32). Given that mitochondria are well-known targets of EtOH (33), and that our previous data have shown suppression of mitochondrial fusion in skeletal muscle by prolonged EtOH exposure (17), we performed experiments to evaluate the effect of chronic EtOH on mitochondrial fusion in cardiomyocytes. We first treated NCVMs in vitro with 50 mM EtOH for 48 h, which represents an in vitro model for chronic alcohol exposure. The EtOH-treated NVCMs exhibited a 40% decrease in mitochondrial continuity and a 75% decrease in mitochondrial fusion activity (Fig. 8*A*).

As an in vivo model, we used EtOH-fed (a 32% EtOH-containing diet for 6–9 mo) and pair-fed rats in which EtOH-induced contractile dysfunction was documented as decreased ejection fraction and fractional shortening (*Materials and Methods*). AVCMs isolated from the EtOH-fed rats showed unaltered resting mitochondrial membrane potential, as assessed by the potentiometric dye TMRE (EtOH: 23 ± 4% uptake, pair-fed: 21 ± 1% uptake; n = 5), though previous studies reported an increased sensitivity to Ca^{2+}-induced depolarization and permeability

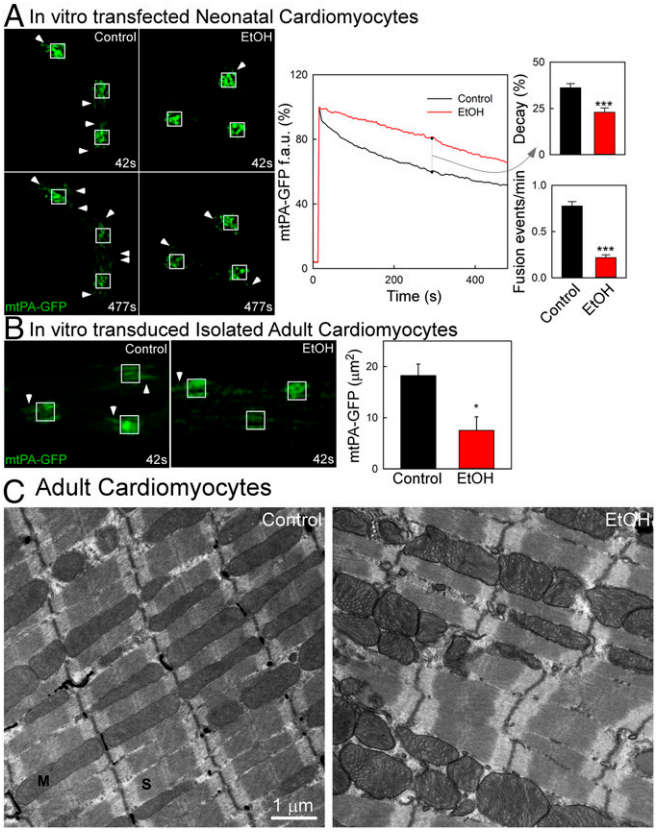

Fig. 8. Effect of prolonged EtOH exposure on cardiac mitochondrial fusion dynamics. (*A*, *Left*) Diffusion of mtPA-GFP in control and EtOH-treated (50 mM for 48 h) NVCMs. Arrowheads indicate diffusion of mtPA-GFP due to pre-established connections (42 s) or newly formed connections due to fusion events (477 s). (*A*, *Center*) mtPA-GFP fluorescence decay in the PA area. (*A*, *Right*) Bar charts showing a greater percentage of decay at 300 s post-PA in control cells (n = 57 ROIs) compared with EtOH-treated cells (n = 59) (*Upper Right*) and a higher fusion event frequency in control cells (n = 63 cells) compared with EtOH-treated cells (n = 33) (*Lower*). (*B*) In vitro-transduced AVCMs from control and EtOH-fed rats (age 6–9 mo). Images of control and EtOH-treated myocytes show limited mtPA-GFP diffusion (arrowheads). Bar charts denote diffusion kinetics for control (n = 12) and EtOH (n = 10), expressed as the area covered by the PA-GFP PA areas. (*C*) Ultrastructure of normal and alcoholic AVCMs. Shown are representative images of longitudinal arrangements of sarcomeres (S) and mitochondria (M).

transition (33, 40). Here we infected in vitro the freshly harvested AVCMs with mtPA-GFP and mtDsRed, and found significantly reduced mitochondrial continuity in the cells derived from the EtOH-fed rats (Fig. 8*B*). We next measured the levels of mitochondrial fusion proteins Mfn1, Mfn2, and Opa1 in mitochondrial fractions of control and EtOH-fed rats. No significant change was detected (Fig. S6), but in three of the five pairs Mfn1 was apparently somewhat decreased in the EtOH-fed rat, suggesting that EtOH can target mitochondrial fusion in the heart without altering the abundance of fusion proteins though a moderate decrease in Mfn1 might be involved.

To further evaluate the dysregulation induced by chronic EtOH exposure, we studied the ultrastructure of mitochondria in the ventricular muscles of hearts harvested from control and EtOH-fed rats (Fig. 8*C*). Mitochondrial cross-sections accounted for 34% and 37% in hearts from control and EtOH-fed animals, respectively (no significant difference); however, the individual mitochondrial cross-section areas in the hearts from EtOH-fed rats showed a tendency for enlargement (control: 0.74 ± 0.14 and EtOH: 0.81 ± 0.15 μm^2, n = 3, P = 0.056). In addition, mitochondria that showed signs of swelling, distortion, and/or resorption of cristae were more prevalent in the cardiac muscles of the EtOH-fed rats (Fig. S7). Using a scoring system for cristae abundance and form ranging from 0 (worst) to 4 (best), the mean score for control was significantly higher in control rats compared with the EtOH-fed rats (2.45 ± 0.23 vs. 1.92 ± 0.2; P < 0.05, paired t test) (Fig. S7*B*). Comparing the prevalence of individual score grades, grade 0 (no well-defined crista) and grade 1 (no crista in >50% of the mitochondrial area) were significantly more prevalent in the EtOH group (Fig. S7*C*). Thus, our results suggest that chronic EtOH consumption causes suppression of mitochondrial fusion activity in cardiac muscle and leads to distortion of the ultrastructure.

Discussion

We have demonstrated that in the adult heart, mitochondria exhibit active fusion dynamics to support matrix content exchange among individual organelles. Distinctively, content exchange among cardiac mitochondria often occurs with slower kinetics compared with that in neonatal heart or in any previously studied cell types. A systematic comparison of freshly isolated and cultured ventricular myocytes revealed that mitochondrial fusion activity decays rapidly when cardiomyocytes are transferred to cell culture. This effect might result from a decrease in contractile activity, as demonstrated by the ability to down-regulate and up-regulate mitochondrial fusion by suppressing and restoring cardiomyocyte contractions, respectively. More specifically, we have shown that oscillatory, but not sustained, Ca^{2+} transients significantly increase mitochondrial fusion frequency in RyR2-expressing HEK cells, suggesting that the Ca^{2+} component of the ECC alone can regulate cardiac mitochondrial communication, and that this mechanism seems to involve Mfn1. Finally, we also have shown that chronic alcohol-fed rats, which exhibit a cardiomyopathy phenotype, show impaired mitochondrial fusion and ultrastructural impairments.

Although mitochondrial fusion has been visualized in diverse differentiated cells, such as neurons (41), hepatocytes (35), and skeletal muscle fibers (17, 18), previous studies of cardiac mitochondrial fusion have been largely confined to evaluating cardiac function after genetic manipulation of the expression of fusion and fission proteins (13, 14, 21, 22). Mitochondrial "kissing" was recently described (16) in cultured AVCMs studied at 48–72 h postisolation. However, our study illuminates the active communication between intermyofibrillar mitochondria in noncultured adult cardiomyocytes, as well as in situ within cardiac muscle. This is a major step forward, because the fusion activity under these conditions is much higher than that in cultured primary cardiomyocytes, indicating that cardiac mitochondrial fusion activity has been underestimated until now.

The lesser mitochondrial continuity and motility observed in cultured AVCMs compared with NVCM is in accordance with our previous observations in differentiated and nondifferentiated cardiac-derived H9c2 cells and in skeletal myoblasts, and indicates decreased mitochondrial continuity and fusion in differentiated striated muscle (17, 42). Mitochondrial fusion is supported by mitochondrial motility, which brings mitochondria into contact to create the opportunity for fusion (7, 38). Multidirectional orientation patterns of microtubules and abundant mitochondrial movements occur in NVCMs (43), H9c2 cells (44), and skeletal myoblasts and myotubes (17). In contrast, in AVCMs and skeletal muscle fibers, mitochondria are spatially confined to the space among the myofilaments and have no opportunity to move toward distant mitochondria. This might account for the lower frequency of fusion events seen in cultured AVCMs and other differentiated muscle paradigms (17, 45). In addition to the structural confinement of mitochondria, in vivo and cell culture conditions seem to affect mitochondrial motility differently, with

mitochondria showing little movement in freshly isolated striated and vascular smooth muscle but vigorous displacement in proliferating cultured striated and smooth muscle cells (17, 46).

Despite the similar fiber organization in adult skeletal muscle fibers and AVCMs, the former exhibit 0.5 fusion event/min, compared with 1.4 fusion events/min in the latter. This difference may be linked to tissue-specific abundance of mitochondrial fusion and fission proteins; however, compared with skeletal muscle, cardiac muscle contains more abundant and larger mitochondria. Unexpectedly, we also found that the fusion-mediated exchange of soluble matrix content shows slower kinetics than that in skeletal muscle and other previously characterized paradigms. Based on our observations and the literature, several factors might explain the unusual complementation kinetics of cardiac mitochondria. First, our evidence for discrete and partial repetitive steps of mtPA-GFP transfer shows a similarity to neurotransmitter release by exocytosis, where fusion of neurotransmitter-filled vesicles with the plasma membrane occurs through partial opening of a fusion pore, leading to a so-called "kiss-and-run" between the membranes, which remain connected via a nanotubule that opens up to a larger pore and then recloses to a nanotube (37). Thus, it might be speculated that the IMM undergoes fast intermittent fusion pore openings as well. Second, the observation of narrow connectors that resemble those previously described in heart mitochondria (16, 34), along with the results of Lavorato et al. (47) showing that in a model of catecholaminergic polymorphic ventricular tachycardia (RyR2-A4860G), nanotunnel structures coupled with slow matrix mixing events become more frequent, support the idea of nanotunnels mediating slow mitochondrial fusion in AVCMs. Third, ample ultrastructural evidence shows that the IMM is highly folded and the numerous cristae define narrow compartments of the matrix specifically in cardiac mitochondria (12, 48, 49), which might have more restricted communication compared with the matrix areas of mitochondria in other tissues. Thus, multiple nonexclusive mechanisms might contribute to the slow content mixing during fusion of heart mitochondria.

A striking observation of the present study is the time-dependent decay in mitochondrial fusion activity when AVCMs are placed into cell culture. The decreases in mitochondrial continuity and fusion activity are accompanied by a previously reported loss of transversal tubules and, consequently, dysregulation of the ECC-associated Ca^{2+} transients (36) and suppressed contractile activity. Therefore, we reasoned that the decay in mitochondrial fusion activity might result from the loss of regular contractile activity or Ca^{2+} transients. Indeed, we found that attenuation of the Ca^{2+} transients and contraction leads to depressed fusion activity, and that stimulation of contraction in cultured AVCMs positively affects mitochondrial fusion activity. Until now, it was thought that in contrast to vesicular fusion, mitochondrial fusion does not depend on Ca^{2+} (50); however, a number of posttranslational modifications regulate mitochondrial dynamics at different levels, including phosphoregulation of Drp1 (51), redox modification of Mfn2 (52), Opa1 proteolytic processing (24), and others. In the heart, mechanical forces and stretch activate various signaling pathways, including such as NADPH-derived ROS, leading to hypertrophy through the activation of diverse signaling programs (53). Whether or not these pathways extended to mitochondrial fusion regulatory proteins was unknown. Our present data show activation of mitochondrial fusion by contraction at both short-term and long-term levels.

An adaptation of mitochondrial communication to persistent contraction is in accordance with previous studies in skeletal muscle showing that exercise enhances the apparent communication among mitochondria (29) and induces expression of mitochondrial fusion proteins (30). Our data show that the amount of the mitochondrial fusion protein Mfn1 decreases in response to a lack of contractile activity in cultured AVCMs, and that the rescue of Mfn1 by exogenous expression in cultured AVCMs leads to a recovery of mitochondrial fusion, highlighting this protein as the key player in striated muscle mitochondrial fusion regulation, in agreement with our previous data in skeletal muscle (17). In contrast to Mfn2, Mfn1 has an exclusive mitochondrial fusion-related function in muscle, whereas Mfn2 is also involved in cardiac mitochondria–SR interactions (26).

We also show that RyR2-dependent oscillatory $[Ca^{2+}]_c$ transients improve mitochondrial connectivity and fusion frequency and also support Mfn1 up-regulation, which may reflect a Ca^{2+}-induced transcriptional regulation. Extensive studies have shown regulation of gene expression by Ca^{2+} in striated muscle and neurons, also known as excitation-transcription coupling (54–56). RyR1- and IP3R-dependent calcium transients differentially control gene expression in skeletal muscle (54). In the heart, IP3R-induced Ca^{2+} transients lead to activation of nuclear factor of activated T cells and hypertrophy (55). Interestingly, repetitive oscillatory Ca^{2+} signals are more efficient than sustained transients for inducing Ca^{2+}-dependent transcriptional factors (57). Along the line of these findings, ECC-evoked Ca^{2+} transients might regulate mitochondrial fusion at a transcriptional level in the heart; however, we also observed a rapidly reversible effect of Ca^{2+} oscillations on the maintenance of mitochondrial fusion activity in HEK-RyR2–expressing cells. This observation, together with the rapid enhancement of mitochondrial fusion activity observed on pacing or spontaneous contractions in AVCMs, suggest a fairly direct and acute positive effect of Ca^{2+} oscillations on mitochondrial fusion.

Given that Mfn1 abundance is unlikely to increase and decrease within minutes, an alternative mechanism must be involved in the acute effect of Ca^{2+} oscillations, such as Ca^{2+}-dependent regulation of mitochondrial metabolism, which is central to fusion activity (20, 58, 59), or Ca^{2+} binding to some components of the fusion machinery or to one of its posttranslational modifiers. Importantly, stopping and restarting of ECC activity does not occur under physiological conditions; thus, we can only claim that the maintenance of mitochondrial fusion activity involves a Ca^{2+} oscillation/contraction-dependent factor in the heart. The potential pathophysiological significance of this factor is highlighted by the work of Lavorato et al. (47), who report that a mutation in RyR2 (A4860G), which alters the normal Ca^{2+} oscillation phenotype, causes a striking change in mitochondrial fusion dynamics.

Several lines of circumstantial evidence implicate mitochondria in either the initiation or progression of cardiomyopathy (60). Mitochondrial involvement in alcoholic cardiomyopathy is intriguing, because mitochondria represent a primary cellular target of alcohol (33). Alcoholic cardiomyopathy is characterized by reduced contractility, along with arrhythmias and fibrosis (61, 62). Alterations in hearts from alcoholic patients at the level of mitochondrial communication were suggested based on early ultrastructural studies (34), and recent studies have reported impairment of mitochondrial DNA integrity by EtOH (63). Given the relevance of mitochondrial fusion to mtDNA stability (5), our results provide a potential structural explanation of these latter findings. A loss of mtDNA integrity was also found in skeletal muscle-conditional knockout of Mfn1 and Mfn2 (64). Moreover, our recent findings in skeletal muscle from alcohol-fed rats show that chronic EtOH consumption leads to inhibition of mitochondrial fusion and mitochondrial calcium uptake efficiency, accompanied by dysregulation of ECC-derived calcium transients, leading to fatigue (17). Our present results indicate that in the heart, alcohol targets mitochondrial dynamic communication via a mechanism that might be linked to the alcohol-induced reduced contractility. Given the apparent bidirectional dependence between contractile and mitochondrial fusion

activities, the pathogenesis of cardiomyopathy might include contractile and mitochondrial fusion impairments that facilitate one another. Based on our findings, it might be speculated that targeting the fusion-fission process may help improve cardiac function in alcoholics.

Materials and Methods

cDNA Constructs and Adenovirus. mtDsRed and mtPA-GFP plasmid DNA have been described previously (7). Type V adenoviruses carrying mtDsRed, mtPA-GFP, LacZ, and mouse Mfn1 were produced by Vector Biolabs.

Cardiac Myocyte Isolation, Cell Lines, and Cultures. NVCMs and AVCMs (14, 65), H9c2 cells, WT cells, and RyR2-overexpressing HEK293T cells (39) were cultured as described in *SI Materials and Methods*.

Animal Treatment. The EtOH-consuming adult male Sprague–Dawley rat model is described elsewhere (17). All procedures were done in accordance with the National Institutes of Health's Guidelines on the Use of Laboratory Animals and were approved by Thomas Jefferson University's Committee on Animal Care. Cardiac function was monitored by echocardiography as described earlier (66). These studies validated significant EtOH-dependent decreases in ejection fraction (EF) and fractional shortening (FF) (EF: control, $78 \pm 2\%$; EtOH, $72 \pm 2\%$; $P < 0.02$; FF: control, $48 \pm 2\%$; EtOH, $43 \pm 2\%$; $P < 0.02$). Thus, in the chronic EtOH-fed rats, contractile dysfunction develops in the heart.

Myocardial Gene Transfer. In vivo adenoviral transformation of adult rat hearts is described in *SI Materials and Methods*.

TEM. Rat hearts were fixed by perfusion of 2.5% (vol/vol) glutaraldehyde in 0.1 M Na-cacodylate buffer (pH 7.4) and stained as described in *SI Materials and Methods*, followed by TEM image acquisition and analysis (17).

Live Cultured Cell Fluorescent Ca^{2+} Imaging and Confocal Microscopy. Fura2-AM–loaded cells were evaluated by epifluorescence microscopy (17). Confocal microscopy imaging of live cells and whole-heart experiments are described in detail in *SI Materials and Methods*.

ACKNOWLEDGMENTS. We thank Emanuel Rubin, Cecilia Hidalgo, Carmen Mannella, Clara Franzini-Armstrong, and David Eisner for helpful discussions; Timothy G. Schneider for transmission electron microscopy (TEM) image acquisition; Valentina Debattisti, Shamim Naghdi, Nadan Wang, and David Weaver for experimental support; and David Booth, Anil Noronha Antony, and Juan Diego Soto for help with setting up data acquisition and presentation. This work was supported by the Pew Latin American Fellows Program in the Biomedical Sciences and the Duchenne Parent Project Netherlands (V.E.), an American Heart Association postdoctoral fellowship (to M.P.), a National Institute on Alcohol Abuse and Alcoholism T32 grant fellowship (to W.S.S.), National Institutes of Health (NIH) Grants AA017773 and DK51526 (to G.H.), and NIH Grants R37 HL061690, P01 HL08806, P01 HL075443, and P01 HK091799 (to W.J.K.).

1. Bers DM (2008) Calcium cycling and signaling in cardiac myocytes. *Annu Rev Physiol* 70:23–49.
2. Maack C, O'Rourke B (2007) Excitation-contraction coupling and mitochondrial energetics. *Basic Res Cardiol* 102(5):369–392.
3. Dedkova EN, Blatter LA (2013) Calcium signaling in cardiac mitochondria. *J Mol Cell Cardiol* 58:125–133.
4. Eisner V, Csordás G, Hajnóczky G (2013) Interactions between sarco-endoplasmic reticulum and mitochondria in cardiac and skeletal muscle: Pivotal roles in Ca^{2+} and reactive oxygen species signaling. *J Cell Sci* 126(Pt 14):2965–2978.
5. Friedman JR, Nunnari J (2014) Mitochondrial form and function. *Nature* 505(7483): 335–343.
6. Shirihai OS, Song M, Dorn GW, 2nd (2015) How mitochondrial dynamism orchestrates mitophagy. *Circ Res* 116(11):1835–1849.
7. Liu X, Weaver D, Shirihai O, Hajnóczky G (2009) Mitochondrial "kiss-and-run": Interplay between mitochondrial motility and fusion-fission dynamics. *EMBO J* 28(20): 3074–3089.
8. Sharma VK, Ramesh V, Franzini-Armstrong C, Sheu SS (2000) Transport of Ca^{2+} from sarcoplasmic reticulum to mitochondria in rat ventricular myocytes. *J Bioenerg Biomembr* 32(1):97–104.
9. Zorov DB, Filburn CR, Klotz LO, Zweier JL, Sollott SJ (2000) Reactive oxygen species (ROS)-induced ROS release: A new phenomenon accompanying induction of the mitochondrial permeability transition in cardiac myocytes. *J Exp Med* 192(7):1001–1014.
10. Aon MA, Cortassa S, O'Rourke B (2006) The fundamental organization of cardiac mitochondria as a network of coupled oscillators. *Biophys J* 91(11):4317–4327.
11. Amchenkova AA, Bakeeva LE, Chentsov YS, Skulachev VP, Zorov DB (1988) Coupling membranes as energy-transmitting cables, I: Filamentous mitochondria in fibroblasts and mitochondrial clusters in cardiomyocytes. *J Cell Biol* 107(2):481–495.
12. Picard M, et al. (2015) Trans-mitochondrial coordination of cristae at regulated membrane junctions. *Nat Commun* 6:6259.
13. Ong SB, et al. (2010) Inhibiting mitochondrial fission protects the heart against ischemia/reperfusion injury. *Circulation* 121(18):2012–2022.
14. Parra V, et al. (2008) Changes in mitochondrial dynamics during ceramide-induced cardiomyocyte early apoptosis. *Cardiovasc Res* 77(2):387–397.
15. Hom JR, Gewandter JS, Michael L, Sheu SS, Yoon Y (2007) Thapsigargin induces biphasic fragmentation of mitochondria through calcium-mediated mitochondrial fission and apoptosis. *J Cell Physiol* 212(2):498–508.
16. Huang X, et al. (2013) Kissing and nanotunneling mediate intermitochondrial communication in the heart. *Proc Natl Acad Sci USA* 110(8):2846–2851.
17. Eisner V, Lenaers G, Hajnóczky G (2014) Mitochondrial fusion is frequent in skeletal muscle and supports excitation-contraction coupling. *J Cell Biol* 205(2):179–195.
18. Luo G, et al. (2013) Defective mitochondrial dynamics is an early event in skeletal muscle of an amyotrophic lateral sclerosis mouse model. *PLoS One* 8(12):e82112.
19. Glancy B, et al. (2015) Mitochondrial reticulum for cellular energy distribution in muscle. *Nature* 523(7562):617–620.
20. Mishra P, Varuzhanyan G, Pham AH, Chan DC (2015) Mitochondrial dynamics is a distinguishing feature of skeletal muscle fiber types and regulates organellar compartmentalization. *Cell Metab* 22(6):1033–1044.
21. Chen Y, Liu Y, Dorn GW, 2nd (2011) Mitochondrial fusion is essential for organelle function and cardiac homeostasis. *Circ Res* 109(12):1327–1331.
22. Kasahara A, Cipolat S, Chen Y, Dorn GW, 2nd, Scorrano L (2013) Mitochondrial fusion directs cardiomyocyte differentiation via calcineurin and Notch signaling. *Science* 342(6159):734–737.
23. Piquereau J, et al. (2012) Down-regulation of OPA1 alters mouse mitochondrial morphology, PTP function, and cardiac adaptation to pressure overload. *Cardiovasc Res* 94(3):408–417.
24. Wai T, et al. (2015) Imbalanced OPA1 processing and mitochondrial fragmentation cause heart failure in mice. *Science* 350(6265):aad0116.
25. Varanita T, et al. (2015) The OPA1-dependent mitochondrial cristae remodeling pathway controls atrophic, apoptotic, and ischemic tissue damage. *Cell Metab* 21(6): 834–844.
26. Chen Y, et al. (2012) Mitofusin 2-containing mitochondrial-reticular microdomains direct rapid cardiomyocyte bioenergetic responses via interorganelle Ca(2+) crosstalk. *Circ Res* 111(7):863–875.
27. Chen Y, Dorn GW, 2nd (2013) PINK1-phosphorylated mitofusin 2 is a Parkin receptor for culling damaged mitochondria. *Science* 340(6131):471–475.
28. Frezza C, et al. (2006) OPA1 controls apoptotic cristae remodeling independently from mitochondrial fusion. *Cell* 126(1):177–189.
29. Picard M, et al. (2013) Acute exercise remodels mitochondrial membrane interactions in mouse skeletal muscle. *J Appl Physiol (1985)* 115(10):1562–1571.
30. Cartoni R, et al. (2005) Mitofusins 1/2 and ERRalpha expression are increased in human skeletal muscle after physical exercise. *J Physiol* 567(Pt 1):349–358.
31. Schiaffino S, Reggiani C (2011) Fiber types in mammalian skeletal muscles. *Physiol Rev* 91(4):1447–1531.
32. Fernández-Solà J (2015) Cardiovascular risks and benefits of moderate and heavy alcohol consumption. *Nat Rev Cardiol* 12(10):576–587.
33. Hajnóczky G, Buzas CJ, Pacher P, Hoek JB, Rubin E (2005) Alcohol and mitochondria in cardiac apoptosis: Mechanisms and visualization. *Alcohol Clin Exp Res* 29(5):693–701.
34. Sudarikova YV, Bakeeva LE, Tsiplenkova VG (1997) Ultrastructure of mitochondrial reticulum of human cardiomyocytes in alcohol cardiomyopathy. *Biochemistry (Mosc)* 62(9):989–1002.
35. Das S, et al. (2012) Mitochondrial morphology and dynamics in hepatocytes from normal and ethanol-fed rats. *Pflugers Arch* 464(1):101–109.
36. Louch WE, et al. (2004) Reduced synchrony of Ca^{2+} release with loss of T-tubules: A comparison to Ca^{2+} release in human failing cardiomyocytes. *Cardiovasc Res* 62(1): 63–73.
37. Mellander LJ, et al. (2014) Two modes of exocytosis in an artificial cell. *Sci Rep* 4:3847.
38. Twig G, et al. (2010) Biophysical properties of mitochondrial fusion events in pancreatic beta-cells and cardiac cells unravel potential control mechanisms of its selectivity. *Am J Physiol Cell Physiol* 299(2):C477–C487.
39. Jiang D, et al. (2004) RyR2 mutations linked to ventricular tachycardia and sudden death reduce the threshold for store-overload-induced Ca^{2+} release (SOICR). *Proc Natl Acad Sci USA* 101(35):13062–13067.
40. Pacher P, Hajnóczky G (2001) Propagation of the apoptotic signal by mitochondrial waves. *EMBO J* 20(15):4107–4121.
41. Berman SB, et al. (2009) Bcl-x L increases mitochondrial fission, fusion, and biomass in neurons. *J Cell Biol* 184(5):707–719.
42. Yi M, et al. (2012) Switch from ER-mitochondrial to SR-mitochondrial calcium coupling during muscle differentiation. *Cell Calcium* 52(5):355–365.
43. Webster DR (1997) Neonatal rat cardiomyocytes possess a large population of stable microtubules that is enriched in post-translationally modified subunits. *J Mol Cell Cardiol* 29(10):2813–2824.
44. Saotome M, et al. (2008) Bidirectional Ca^{2+}-dependent control of mitochondrial dynamics by the Miro GTPase. *Proc Natl Acad Sci USA* 105(52):20728–20733.
45. Nishimura S, et al. (2006) Microtubules modulate the stiffness of cardiomyocytes against shear stress. *Circ Res* 98(1):81–87.

46. Chalmers S, et al. (2012) Mitochondrial motility and vascular smooth muscle proliferation. *Arterioscler Thromb Vasc Biol* 32(12):3000–3011.
47. Lavorato M, et al. (2017) Increased mitochondrial nanotunneling activity, induced by calcium imbalance, affects intermitochondrial matrix exchanges. *Proc Natl Acad Sci USA*, 10.1073/pnas.1617788113.
48. Mannella CA, Lederer WJ, Jafri MS (2013) The connection between inner membrane topology and mitochondrial function. *J Mol Cell Cardiol* 62:51–57.
49. Riva A, Tandler B, Loffredo F, Vazquez E, Hoppel C (2005) Structural differences in two biochemically defined populations of cardiac mitochondria. *Am J Physiol Heart Circ Physiol* 289(2):H868–H872.
50. Liu X, Hajnóczky G (2009) Ca^{2+}-dependent regulation of mitochondrial dynamics by the Miro-Milton complex. *Int J Biochem Cell Biol* 41(10):1972–1976.
51. Cereghetti GM, et al. (2008) Dephosphorylation by calcineurin regulates translocation of Drp1 to mitochondria. *Proc Natl Acad Sci USA* 105(41):15803–15808.
52. Shutt T, Geoffrion M, Milne R, McBride HM (2012) The intracellular redox state is a core determinant of mitochondrial fusion. *EMBO Rep* 13(10):909–915.
53. Pimentel DR, et al. (2001) Reactive oxygen species mediate amplitude-dependent hypertrophic and apoptotic responses to mechanical stretch in cardiac myocytes. *Circ Res* 89(5):453–460.
54. Valdés JA, et al. (2007) NF-kappaB activation by depolarization of skeletal muscle cells depends on ryanodine and IP3 receptor-mediated calcium signals. *Am J Physiol Cell Physiol* 292(5):C1960–C1970.
55. Wu X, et al. (2006) Local InsP3-dependent perinuclear Ca^{2+} signaling in cardiac myocyte excitation-transcription coupling. *J Clin Invest* 116(3):675–682.
56. Ma H, Groth RD, Wheeler DG, Barrett CF, Tsien RW (2011) Excitation-transcription coupling in sympathetic neurons and the molecular mechanism of its initiation. *Neurosci Res* 70(1):2–8.
57. Dolmetsch RE, Xu K, Lewis RS (1998) Calcium oscillations increase the efficiency and specificity of gene expression. *Nature* 392(6679):933–936.
58. Wai T, Langer T (2016) Mitochondrial dynamics and metabolic regulation. *Trends Endocrinol Metab* 27(2):105–117.
59. Mishra P, Chan DC (2016) Metabolic regulation of mitochondrial dynamics. *J Cell Biol* 212(4):379–387.
60. Dorn GW, 2nd (2015) Mitochondrial dynamism and heart disease: Changing shape and shaping change. *EMBO Mol Med* 7(7):865–877.
61. Vendemiale G, et al. (2001) Mitochondrial oxidative damage and myocardial fibrosis in rats chronically intoxicated with moderate doses of ethanol. *Toxicol Lett* 123(2-3): 209–216.
62. Ponnappa BC, Rubin E (2000) Modeling alcohol's effects on organs in animal models. *Alcohol Res Health* 24(2):93–104.
63. Laurent D, et al. (2014) Chronic ethanol consumption increases myocardial mitochondrial DNA mutations: A potential contribution by mitochondrial topoisomerases. *Alcohol Alcohol* 49(4):381–389.
64. Chen H, et al. (2010) Mitochondrial fusion is required for mtDNA stability in skeletal muscle and tolerance of mtDNA mutations. *Cell* 141(2):280–289.
65. Sheu SS, Sharma VK, Banerjee SP (1984) Measurement of cytosolic free calcium concentration in isolated rat ventricular myocytes with quin 2. *Circ Res* 55(6):830–834.
66. Pleger ST, et al. (2005) S100A1 gene therapy preserves in vivo cardiac function after myocardial infarction. *Mol Ther* 12(6):1120–1129.
67. Antony AN, et al. (2016) MICU1 regulation of mitochondrial Ca(2+) uptake dictates survival and tissue regeneration. *Nat Commun* 7:10955.
68. Roy SS, Hajnóczky G (2009) Fluorometric methods for detection of mitochondrial membrane permeabilization in apoptosis. *Methods Mol Biol* 559:173–190.
69. Drazner MH, et al. (1997) Potentiation of beta-adrenergic signaling by adenoviral-mediated gene transfer in adult rabbit ventricular myocytes. *J Clin Invest* 99(2): 288–296.

Supporting Information

Eisner et al. 10.1073/pnas.1617288114

SI Materials and Methods

Cardiac Myocyte Isolation and Culture. NVCMs were cultured in F-10 Ham medium supplemented with 10% HS, 5% FBS (Invitrogen), and penicillin/streptomycin as described previously (14). The NVCMs were plated on top of 2% (wt/vol) gelatin-coated glass coverslips at a density of 5×10^5 cells per 35-mm dish. AVCMs were isolated from 2- to 10-mo-old rats (65) and plated on laminin (Roche)-coated coverslips in M199 complete medium (0.2% BSA, 5 mM taurine, 2.5 mM creatine, 2 mM carnitine, and 1× insulin-transferrin-selenium; Invitrogen) containing 1 mM BDM. Both NVCMs and AVCMs were cultured at 37 °C with atmospheric air and 5% CO_2. Fluorometric measurements of the mitochondrial membrane potential were performed in permeabilized AVCMs as described previously (67, 68).

Cell Lines and Cultures. H9c2 cells of passage 36–40 were grown in low-glucose DMEM (Thermo Fisher Scientific) containing sodium pyruvate and 10% FBS (Thermo Fisher Scientific), supplemented with penicillin/streptomycin (Lonza), L-glutamine (Thermo Fisher Scientific), and additional sodium pyruvate (Sigma-Aldrich). WT HEK293T cells and Flp-in HEK293T cells overexpressing RyR2 (39) were grown in DMEM and 10% FBS, supplemented with penicillin/streptomycin and L-glutamine. When induction of RyR2 was desired, 1 μg/mL tetracycline (Sigma-Aldrich) was applied.

Myocardial Gene Transfer. Male Sprague–Dawley rats (150–180 g) were anesthetized with 2–3% isofluorane. A small skin incision was made in the left front chest. After dissecting pectoral muscles, exposing the ribs, and externalizing the heart through the fourth intercostal space, multiple-point left ventricular free wall injections were performed with an insulin syringe (30g needle). The syringe carried 180 μL of mtDsRed and mtPA-GFP mixed adenoviral particles (ratio, 1:2). Immediately after gene delivery, the heart was placed back into the thoracic cavity, followed by suturing of the ribs and skin. The procedure took less than 2 min. The animal were returned to their cages and were given appropriate analgesia. At 6–8 d after the surgery, the animals were killed, and hearts were harvested for whole-heart imaging or myocyte isolation. No damage to or change in viability of AVCMs was observed after adenovirus injection (69).

In Vitro Transfection and Transduction of Cardiomyocytes. At 18 h after plating, the NVCMs were incubated with Optimem (Invitrogen) for 6 h and then transfected with a 1:1 mix of mtDsRed and mtPA-GFP (total 4 μg of DNA) and Lipofectamine 2000 at 1 mL per dish. After overnight incubation, the medium was replaced by 0.5% FBS–F-10 Ham medium supplemented with 20 μM 5-bromo-2′-deoxyuridine (Sigma-Aldrich).

Freshly isolated AVCMs were in vitro-transformed with a 1:1 mixture of AdmtDsRed and AdmtP-GFP (a total of 7×10^8 pfu per 35-mm dish) in 1 mL of 0.1% BSA-M199 medium, supplemented with antibiotics and 1 mM BDM. Freshly isolated in vivo-infected AVCMs were in vitro-transformed with AdMfn1 (7×10^8 pfu per 35-mm dish) or AdLacZ (5.7×10^7 or 2.4×10^7 pfu per 35-mm dish) in 1 mL of 0.1% BSA-M199 medium, supplemented with antibiotics and 1 mM BDM. After overnight incubation, the medium was replaced by M199 complete medium.

Transfection of H9c2 and HEK293T Cells. Cells were plated on poly-D-lysine (EMD Millipore)-coated 25-mm glass coverslips (Thermo Fisher Scientific) in 1.8 mL of medium in 35-mm tissue culture dishes (Falcon; Corning). At 24 h after plating, cells were transfected with a 1:1 mix of mtDsRed and mtPA-GFP in solution (total of 2 μg of DNA) diluted with 6 μL of XTremeGene9 (Fugene; Roche) in 200 μL of Opti-MEM (Thermo Fisher Scientific). Imaging was performed at 24–48 h after the transfection.

In Vitro Chronic Alcohol Exposure. At 24 h after plating, NVCMs were treated with 0.3% vol/vol 50 mM EtOH for 48 h. Culture dishes were placed in a 100-mm dish containing 1% ethanol/water solution to maintain an alcohol-rich atmosphere. EtOH was renewed every 12–24 h.

Short-Term Field Stimulation. Cardiomyocytes were field-stimulated with 2-Hz pulses of 2-ms each, for 5 min in a custom-made chamber (2 mL, with two parallel platinum electrodes positioned on each side of the light path, 1 cm apart) connected to a square pulse stimulator and an oscilloscope. Cells were perfused with a 0.25% BSA $CaCl_2$-containing solution during electrostimulation. Cells were tested for electric pulse-induced contractile activity, stimulated for 5 min with perfusion, and imaged for another 5 min. Control cells were perfused without electrostimulation for 5 min and then imaged for another 5 min.

Western Blot Analysis. Here 30 μg of membrane-enriched fractions were loaded onto each lane of an 8% SDS/PAGE. Primary antibodies for Mfn1 (kindly provided by Dr. Richard Youle, National Institutes of Health), Mfn2 (Sigma-Aldrich), Opa1 (BD Biosciences), COX IV (Cell Signaling Technology), and Prohibitin (Abcam) were used. Bound antibodies were detected by chemiluminescence or IRDye 800 secondary antibodies (LI-COR Biosciences).

Transmission Electron Microscopy. Rats were injected with 1,000 U of heparin i.p. 15 min before induction of anesthesia with nembutal, followed by opening of the chest and cannulation of the aorta with an 18-1/2g i.v. cannula for in situ washing of the coronary arteries with oxygenated Ringer's solution supplemented with 0.1% procaine for 3–5 min at a perfusion rate of 40 mL/min. Subsequently, the perfusate was switched to 2.5% (vol/vol) glutaraldehyde in 0.1 M Na-cacodylate buffer (pH 7.4). All perfusates were maintained at 4 °C. The ventricle was subsequently cut into $<2 \times 2$-mm pieces and kept in the fixative solution at 4 °C for 2 h. The samples were then washed with 0.1 M Na-cacodylate buffer and postfixed with partially reduced osmium tetroxide (2% OsO_4 and 0.8% potassium ferrocyanide in 0.1 M Na-cacodylate) overnight. Multiple washing steps with water were followed by en bloc staining with 1% uranyl acetate for 1 h at 4 °C. Stained samples were dehydrated on an acetone dilution series and embedded in Spurr's resin (Electron Microscopy Sciences) according to the manufacturer's instructions. Sectioning, image acquisition, and analysis were performed as described previously (17).

Live Cultured Cell Fluorescent Ca^{2+} Imaging. For imaging of $[Ca^{2+}]_c$, the cells were first loaded with 2 μM Fura2-AM (Life Technologies) for 20 min at room temperature in 2.0% (wt/vol) BSA ECM, in the presence of 0.003% pluronic acid and 100 μM sulfinpyrazone. After dye loading, the coverslip was mounted to a heated (35 °C) incubator chamber in ECM containing 0.25% BSA and sulfinpyrazone. Detection of Fura2 fluorescence (excitation, 340 and 380 nm; emission, 540/50 nm) was achieved using an inverted microscope (40×, DMRE 2; Leica), UApo objective (Olympus), and a CCD camera (ProEM 1024 EMCCD

camera, MultiFluo system; Princeton Instruments). Image duplets (excitation, 340 and 380 nm for Fura2) were obtained every 3 s for 10 min. For H9c2 cells, treatment with 60 mM KCl or 5 μM ionomycin was applied at image 10.

Image Analysis. Image analysis was done using custom-designed Spectralyzer software or Zen 2010 (Carl Zeiss). Mitochondrial matrix continuity was evaluated via two approaches using Fiji. Spreading of mtPA-GFP from the area of photoactivation was evaluated by masking the 5 × 5-μm photoactivation areas and quantifying the time-dependent decay in fluorescence intensity. Alternatively, the entire area outside the photoactivated areas was masked. The images were thresholded using Fiji, and every pixel outside the PA area that exceeded the threshold by >10% was included in the mtPA-GFP area of spreading. Fusion events/min = #fusion events × 3 ROIs/#ROIs/min, unless stated differently.

Confocal Microscopy. Imaging of isolated cells was performed in a 0.25% BSA ECM consisting of 121 mM NaCl, 5 mM $NaHCO_3$, 4.7 mM KCl, 1.2 mM KH_2PO_4, 1.2 mM $MgSO_4$, 2 mM $CaCl_2$, 10 mM glucose, and 10 mM Na-Hepes, pH 7.4, at 35 °C. During the experiments, 10 mM BDM was added unless indicated otherwise. Image acquisition (LSM 780 NLO laser scanning microscope with GASP detectors; Carl Zeiss) was performed with excitation at 488 nm (mtPA-GFP) and 568 nm (mtDsRed) using a 63×/1.4 NA ApoPlan objective. PA-GFP was photoactivated in a two-photon mode using a Chameleon pulsed laser system (760 nm; Coherent). To create 3D-like reconstructions, a sequence of images was collected starting below the adherent surface and moving upward in 0.367-μm steps (18 steps). Imaging of H9c2 cells was performed in 2D in the same fashion. Cells were treated before imaging with 60 mM KCl or 5 μM ionomycin, or left untreated (control). A series of 125 images was obtained from each cell, with one image recorded every 4 s.

For whole-heart imaging, rats were injected i.p. with 1,000 U of heparin 15 min before being anesthetized with isofluorane 3–5%. The heart was isolated and cannulated through the aorta with a 16g needle, followed by immediate reverse perfusion using a Langerdoff system with 37 °C carbogen pre-equilibrated $CaCl_2$-free Joklik's medium (Lonza) for 6 min. When needed, TMRE (100 nM) was added during perfusion with the Joklik's medium. The heart was then quickly transferred and connected to perfusion pump-fed tubing. Before imaging, the heart was perfused for 10 min with $CaCl_2$-free 0.25% BSA ECM supplemented with 10 mM BDM and 100 μM EGTA. During imaging, which took <7 min, the perfusion was stopped to avoid movement artifacts. Perfusion was continued between imaging periods. Imaging was performed as described for isolated cells using a 100× water objective.

For simultaneous study of the Ca^{2+} oscillations and GFP spreading, HEK293T cells transfected with mtDsRed and mtPA-GFP as described previously were loaded with 1.5 μM Fluo8-AM (TEFLabs) for 20 min at 37 °C in 2.0% (wt/vol) BSA ECM in the presence of 0.003% pluronic acid and 100 μM sulfinpyrazone. Imaging was performed in 0.25% BSA ECM and 100 μM sulfinpyrazone at 35 °C. Fluo8 was excited at 488 nm, and mtDsRed and mtPA-GFP were excited and bleached, respectively, as described previously. Fluo8 fluorescence was masked in the nuclear area.

Statistics. Data are reported as mean ± SE. The significance of differences was calculated using Student's *t* test or the Mann–Whitney rank-sum test.

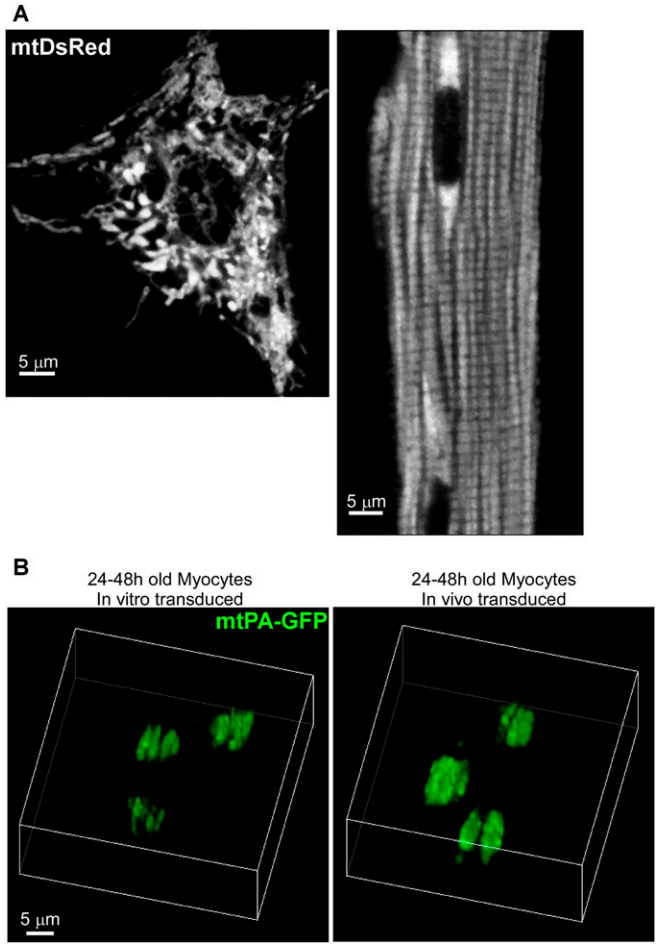

Fig. S1. Mitochondrial morphology in neonatal and adult cardiac myocytes and 3D reconstruction of mitochondria in cultured myocytes. (*A*) Cultured NVCMs and in vivo-transformed freshly isolated AVCMs expressing mitochondrial targeted DsRed. The two cells show significant differences in morphology as well as in mitochondrial distribution, size, and density. (*B*) A 3D reconstruction of mtPA-GFP PA regions (5 × 5 μm) and surrounding areas of 24- to 48-h-old myocytes transduced in vitro (*Left*) or in vivo (*Right*) at 8 min after PA.

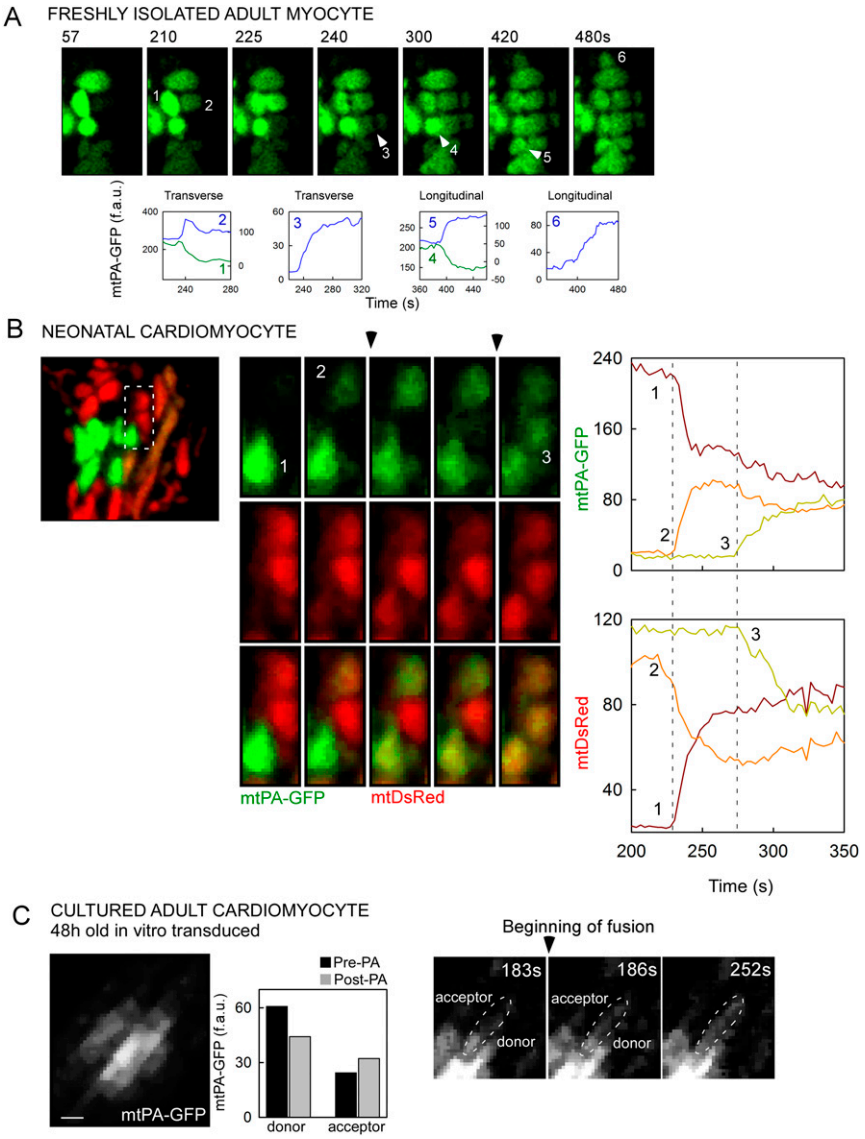

Fig. S2. Examples of mitochondrial fusion events. (*A*) Diverse orientation fusion events in freshly isolated in vivo-transformed AVCMs. (*Upper*) Images of time series showing sequential fusion events in both transverse and longitudinal orientations. (*Lower*) Quantitative evaluation of mtPA-GFP fluorescence transfer between numbered organelles. (*B*) Sequential mitochondrial fusion events in NCVMs. (*Left*) A 5 × 5-μm region of mtPA-GFP PA. (*Center*) Zoom-in view of the rectangle denoted by the white-dashed line showing the time course of mitochondrial fusion events between mitochondria 1 and 2, followed by matrix mixing between mitochondria 2 and 3. (*Right*) Quantification of mtPA-GFP fluorescence transfer from donor 1 to acceptor 2, and concomitant mixing of mtDsRed from 2 to 1 (the latter was photobleached when mtPA-GFP was photoactivated by 2P illumination). At 100 s after the first event, a new two-way mitochondrial mixing is evidenced between mitochondria 2 and 3. (*C*) Mitochondrial fusion event in an in vitro- transformed, 48-h–cultured AVCM. (*Upper*) The area of PA. (*Lower*) Time series of a fusion event between two neighbor mitochondria. Quantification of mtPA-GFP mixing is shown in the bar chart, highlighting the changes in the PA-GFP levels between donor and acceptor mitochondria before and after the fusion event.

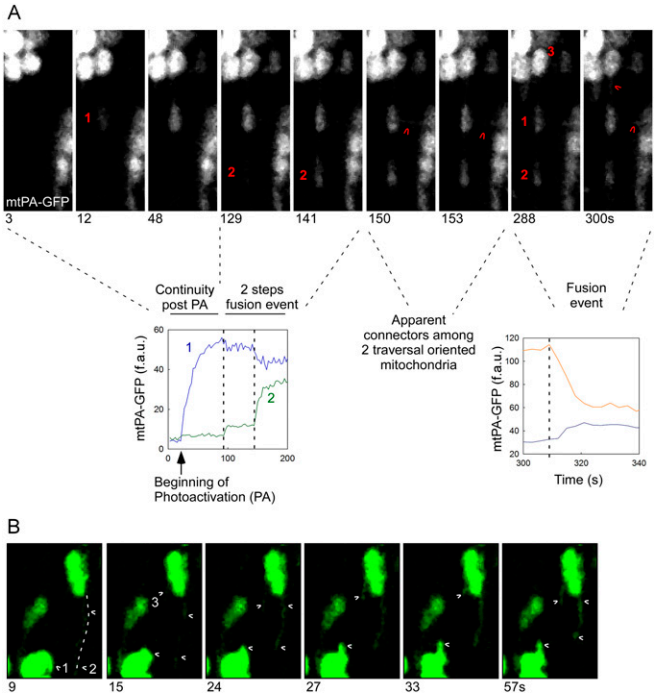

Fig. S3. Diverse fusion events in AVCMs. (*A*) Diversity of newly formed mitochondrial communications by means of fusion events. A fusion event starts when an mtPA-GFP donor mitochondrion reaches a non-neighbor acceptor (1) through an apparent narrow connector. The kinetics of this event are very slow. Next, mitochondrion 1 partially equilibrates its mtPA-GFP matrix content through an additional fusion event with mitochondrion 2. Note that mitochondria 1 and 2 are also apparently connected through a narrow structure. Moreover, transversally oriented connectors become evident between mitochondrion 1 and a transversally oriented mitochondrion. Finally, at 288 s post-PA, a new fusion event occurs between mitochondria 1 and 2, fully equilibrating their contents. Thus, this example indicates that heart mitochondria can use narrow connectors to exchange their contents, and that two organelles can undergo partial and then complete fusion events, suggesting the partial opening of fusion pores or incomplete fusion events, followed by fission and then fusion again. (*B*) An emerging nanotunnel in a freshly isolated AVCM. Dynamic tubular mitochondria appear to emerge from globular organelles. (*Upper Left*) Two PA regions. (*Upper Right*) A region in which apparent nanotunnels emerge from globular mitochondria. For mitochondria movement activity, red indicates negative changes, and blue indicates positive changes. (*Lower*) Time-lapse images of elongated mitochondria (2 and 3) emerging and retracting from one large globular mitochondrion, as shown in Movie S8. In addition, elongated mitochondrion 1 moves around another globular mitochondrion.

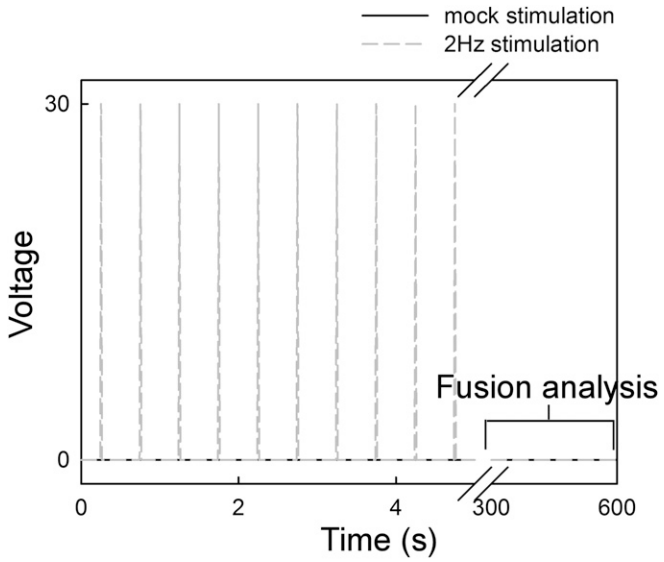

Fig. S4. Pacing scheme applied in Fig. 5*D*. Freshly isolated in vivo-transformed ventricular myocytes plated on top of laminin-coated coverslips were mounted in a custom-made chamber equipped with platinum electrodes. At the confocal microscope stage, the chamber was connected to a Grass stimulator, and 2-Hz square-shaped pulses were triggered (30 V, 2 ms) for 5 min. The stimulation buffer was 0.25% BSA $CaCl_2$ without BDM. After brief and careful washing, and loading of the same experimental chamber with 10 mM BDM-supplemented 0.25% BSA ECM, fusion events were evaluated for 5 min. Mock experiments involved the same treatment of the cells without field stimulation.

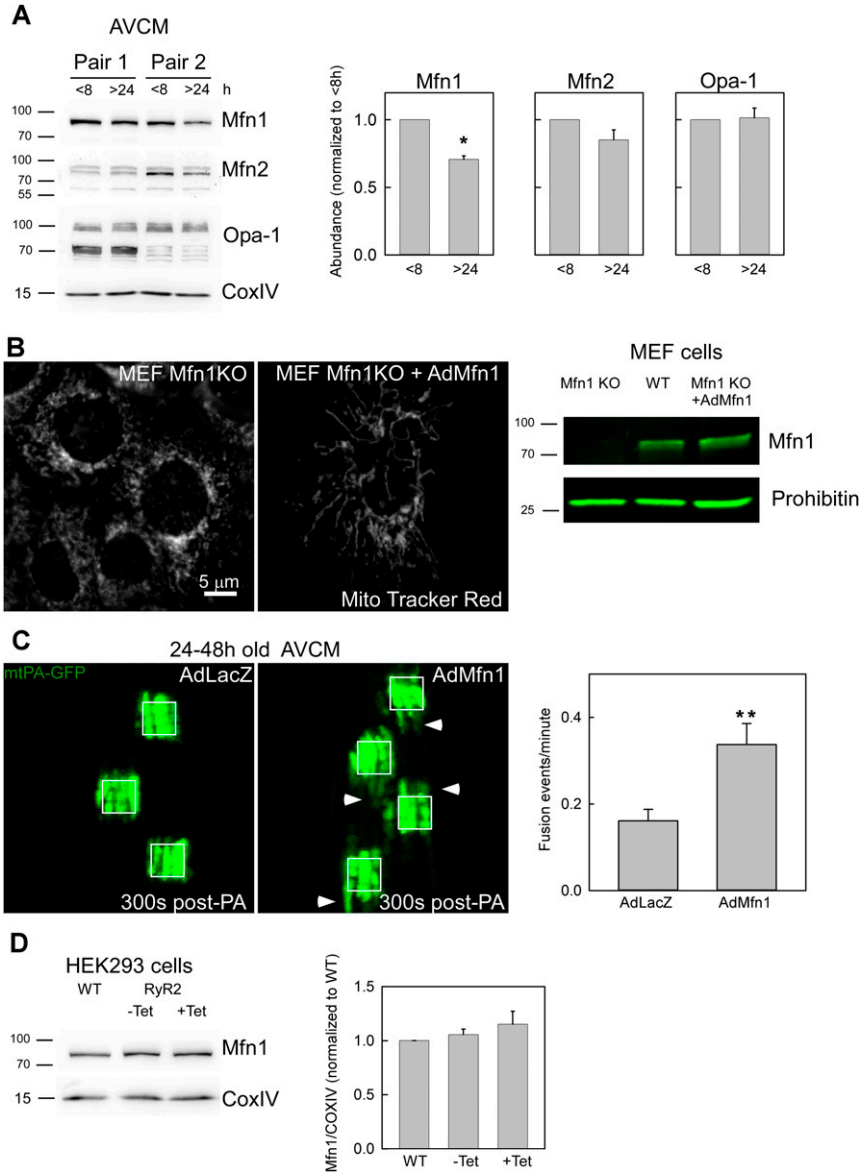

Fig. S5. Mitochondrial fusion protein Mfn1 decays in cultured AVCMs and rescues fusion upon exogenous expression. (*A*) Freshly isolated AVCMs were plated on culture dishes for 2–8 h or kept in culture for at least 24–30 h. Samples were snap-frozen, and membrane extract was prepared for Western blot analysis and tested with the indicated antibodies. Specific bands were quantified with regard to the <8-h condition. $n = 4$ independent experiments. $P < 0.05$. (*B*) Mfn1 KO cells were transduced with AdMfn1, and at 24–28 h after infection, the cells were loaded with MitoTracker Red and evaluated by confocal microscopy (*Left*). Cell membrane extracts were evaluated by Western blot analysis to determine the abundance of Mfn1 in MEF WT, Mfn1 KO, and Mfn1 KO cells transduced with AdMfn1 (*Right*). Transformation of Mfn1 KO cells with AdMfn1 rescued the expression of Mfn1. (*C*) AdmtPA-GFP and AdmtDsRed in vivo-infected AVCMs were infected in vitro with either control AdLacZ or AdMfn1 virus and then evaluated at 24–48 h after plating. The white squares represent 25-μm^2 regions. (*Left*) Representative images of mtPA-GFP spreading at 300 s post-PA shows increased mitochondrial continuity for AdMfn1 transformed cells compared with control, as indicated by white arrowheads. (*Right*) Quantification of mitochondrial fusion for the LacZ- and Mfn1-infected AVCMs shows an increase in mitochondrial fusion for Mfn1 cells ($n = 39$) compared with LacZ cells ($n = 40$). $^{**}P < 0.01$. (*D*) WT and RyR2-HEK293T cells noninduced or induced for 48 h with tetracycline (Tet) were used to prepare membrane-enriched extracts, which were evaluated on 8% PAGE and tested for Mfn1 protein levels. $n = 2$ independent experiments.

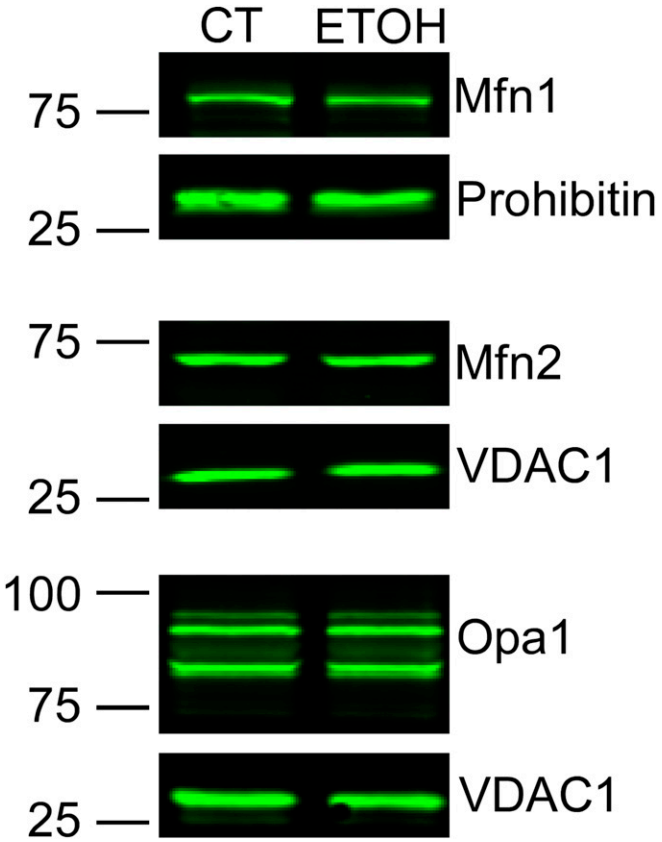

Fig. S6. Abundance of mitochondrial fusion proteins in control and EtOH-fed cardiac mitochondria. Shown is a representative Western blot of mitochondrial fusion proteins tested in rat heart mitochondrial extracts from control and EtOH-fed animals. Mfn1 and Mfn2 ($n = 5$ pair) and Opa1 ($n = 2$ pair) were tested.

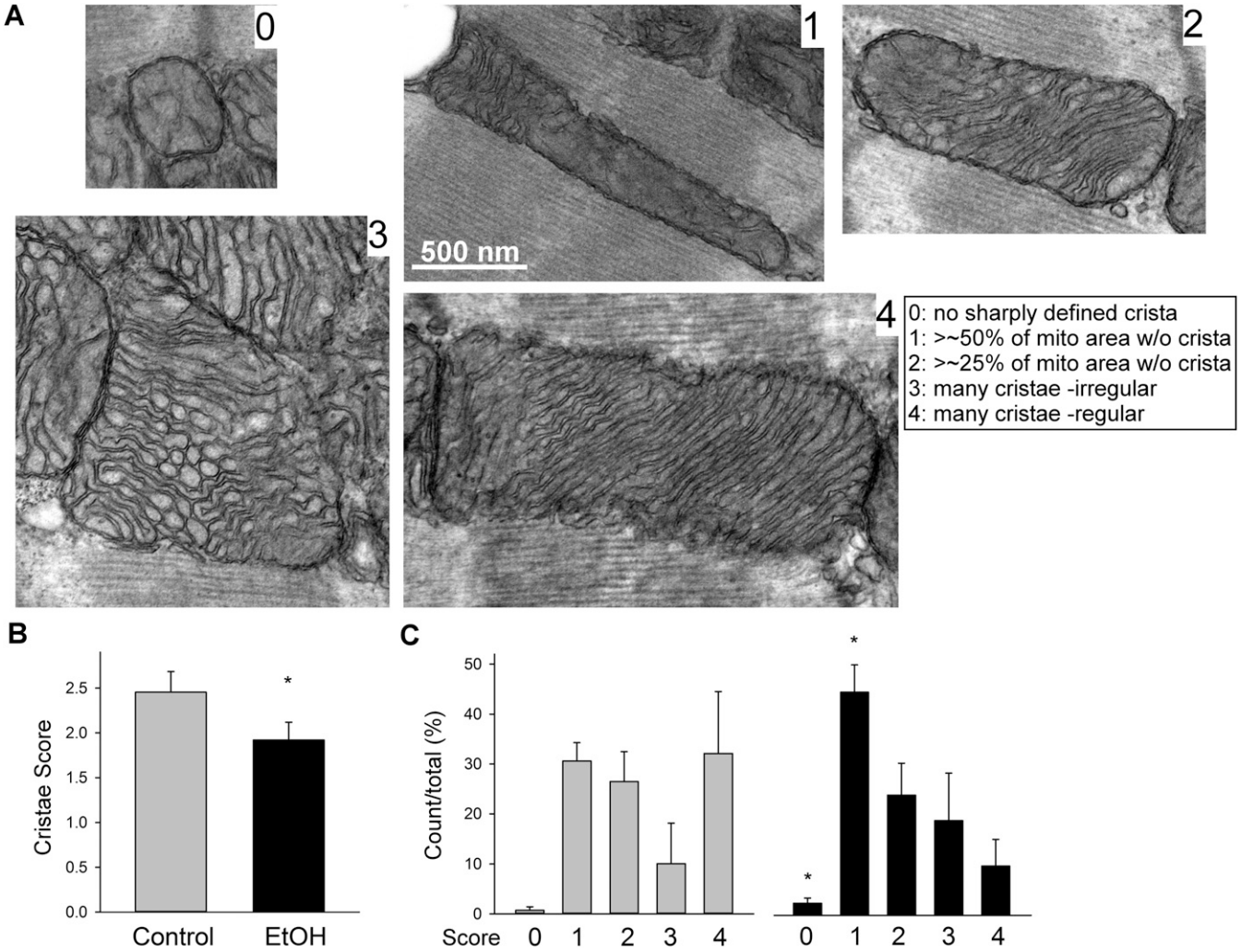

Fig. S7. Higher prevalence of abnormal IMM folding with absent and/or irregular cristae in the cardiac mitochondria of the EtOH-fed rats. (*A*) Mitochondrial cristae morphology analysis in TEM images of longitudinally sectioned left ventricular wall samples. To quantitate potential alterations, a five-grade scoring system for cristae abundance and form in individual mitochondria was introduced as illustrated. (*Inset*) Example images for each grade and definition of the grades. (*B* and *C*) Bar graphs showing the cumulated overall mean scores (*B*) and the prevalence of the individual score grades across the analyzed mitochondrial population for each pair of animals (*C*). For one pair in which membrane contrast was exceptionally good, the analysis was performed by comparing a total of 179 mitochondria in five fields of 11 × 11 μm (4,400× direct magnification). For the other two pairs, higher magnification was needed. The number of mitochondria compared was 42 controls (32 2.3 × 2.3 μm and 3.2 × 3.2 μm fields at 21,000× and 15,000×) vs. 68 EtOH (23 3.2 × 3.2-μm fields) and 36 controls (24 2.3 × 2.3-μm fields) vs. 73 EtOH (32 fields ranging between 4.5 × 4.5 μm and 2.3 × 2.3 μm at 11,000–21,000× direct magnification).

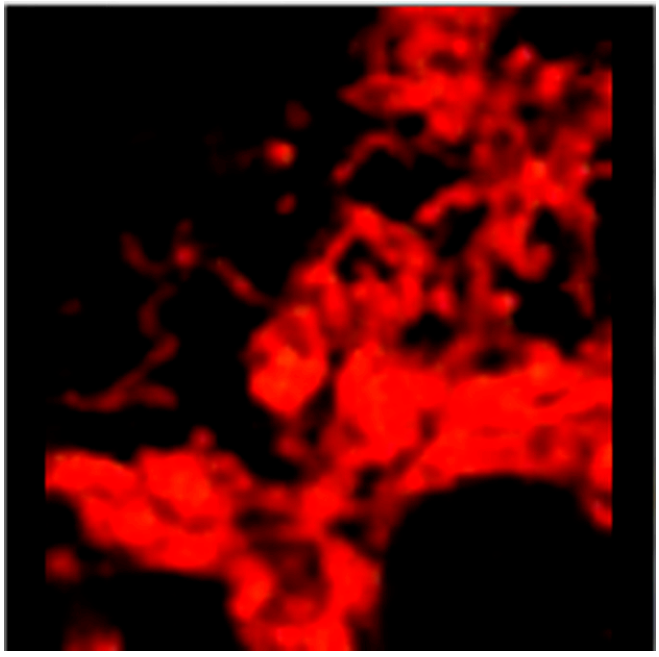

Movie S1. A subregion of an NVCM expressing mtDsRed and mtPA-GFP. On photoactivation of mtPA-GFP by means of 2P within a 5 × 5 μm region, mitochondrial continuity, fusion, and motility are evidenced by mtPA-GFP spreading, newly formed mitochondrial communications, and displacement, respectively. This 7-min video (frequency acquisition, 0.25 Hz, at 7 fps) shows highly active mitochondrial dynamics.

Movie S1

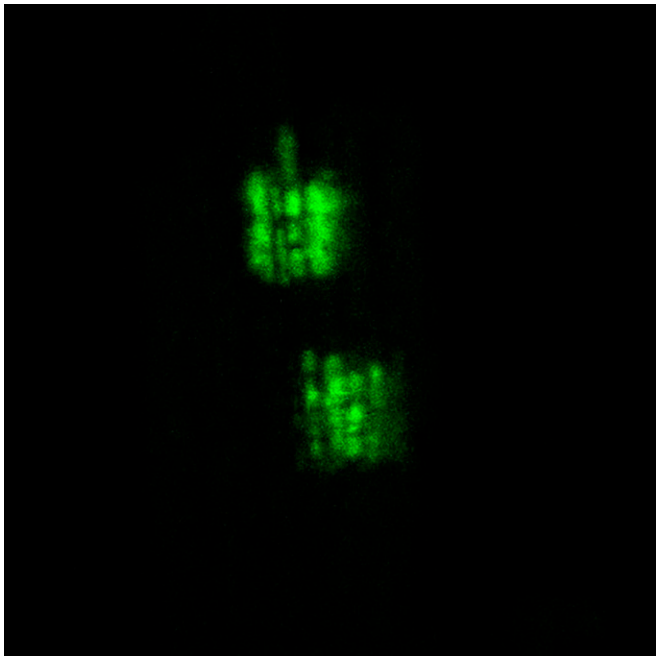

Movie S2. Mitochondrial dynamics in 24–48 h in vitro-transformed AVCMs expressing mtPA-GFP. mtPA-GFP was photoactivated in 2 5 × 5-μm regions, and the fluorescence spreading and newly formed communications among mitochondria were followed for 8.25 min. Frequency acquisition, 0.33 Hz, at 7 fps.

Movie S2

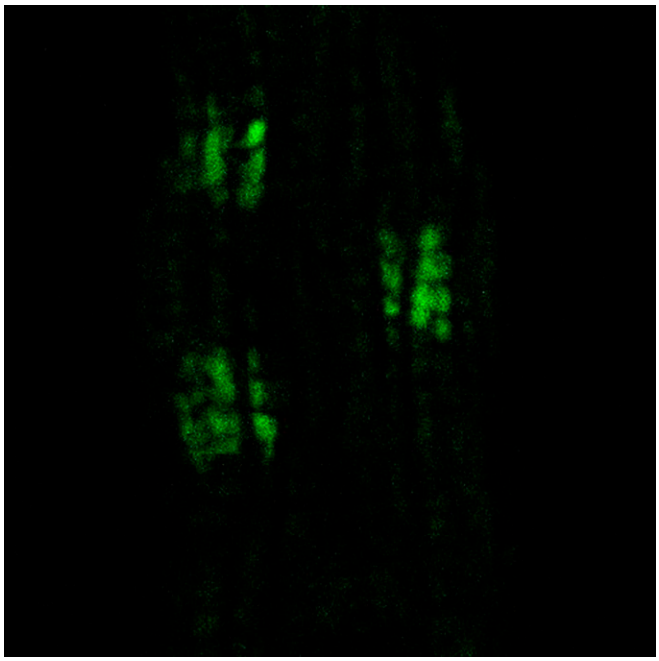

Movie S3. Mitochondrial dynamics in 24–48 h in vivo-transformed AVCMs expressing mtPA-GFP. mtPA-GFP was photoactivated in 3 5 × 5-μm regions, and the fluorescence spreading and newly formed communications among mitochondria were followed for 8.25 min. Frequency acquisition, 0.33 Hz, shown at 7 fps.

Movie S3

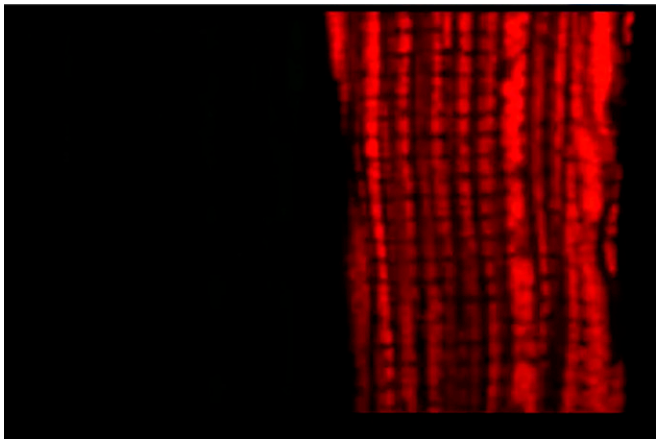

Movie S4. Mitochondrial dynamics in a freshly isolated in vivo-transformed AVCMs expressing mtDsRed and mtPA-GFP. mtPA-GFP was photoactivated in 5 5 × 5-μm regions, and the fluorescence spreading and newly formed communications among mitochondria were followed for 7 min. Frequency acquisition, 0.25 Hz, shown at 7 fps.

Movie S4

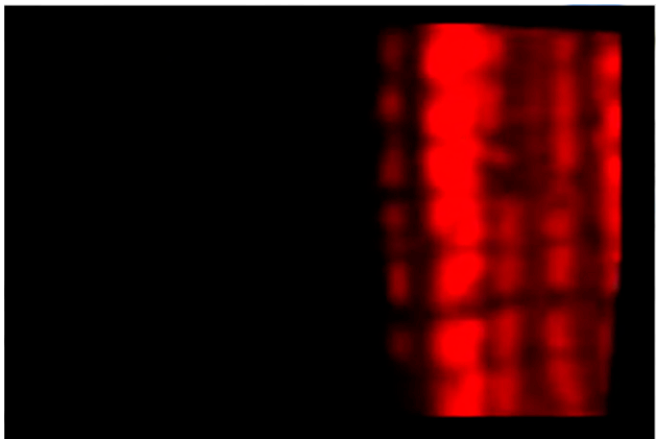

Movie S5. A subregion of a freshly isolated in vivo-transformed AVCM expressing mtDsRed and mtPA-GFP. Photoactivation of mtPA-GFP by means of 2P illumination within a 5 × 5-μm region. Mitochondrial continuity and fusion are evidenced by continuous and abrupt mtPA-GFP spreading, respectively. Video duration, 8.25 min; acquisition frequency, 0.33Hz, shown at 7 fps.

Movie S5

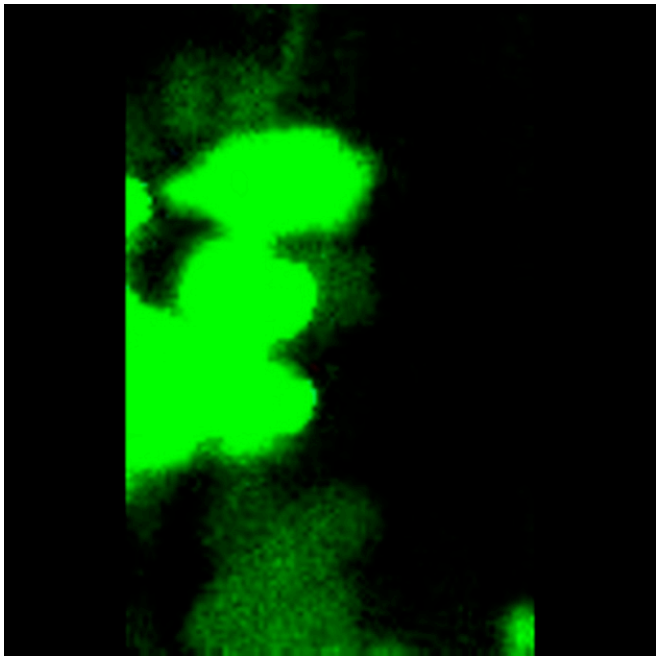

Movie S6. Sequential mitochondrial fusion events in a freshly isolated in vivo-transformed AVCM. mtPA-GFP mixing in transverse and longitudinal orientations indicates mitochondrial fusion events in a region contiguous with a PA area. Video duration, 8.25 min; acquisition frequency, 0.33 Hz, shown at 7 fps.

Movie S6

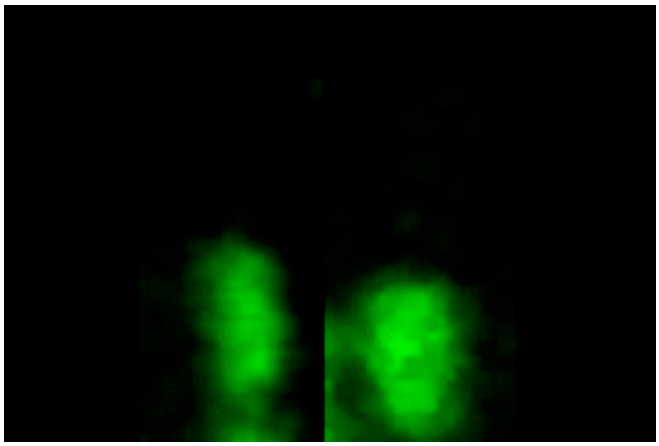

Movie S7. Fast and slow kinetics of AVCM fusion events. Parallel videos showing representative examples described in Fig. 3, highlighting fast and slow fusion mixing kinetics. Each video lasts 300 s; acquisition frequency, 0.33Hz, at 7 fps.

Movie S7

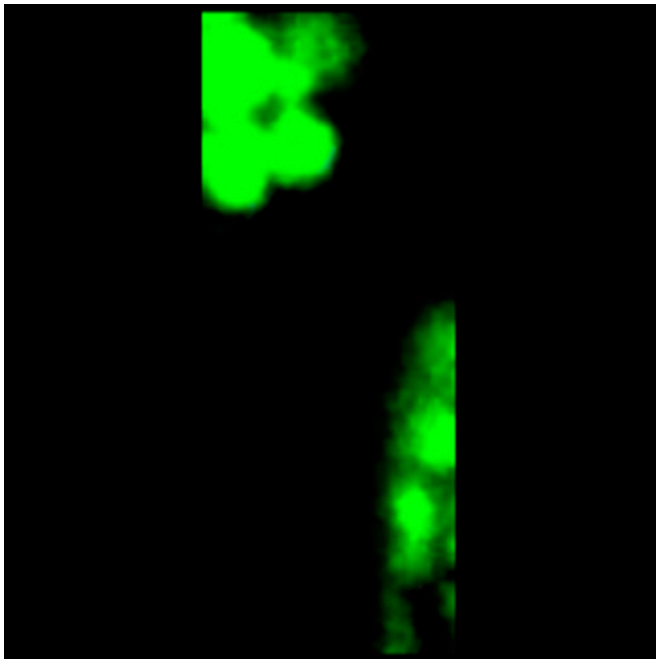

Movie S8. Diverse mitochondrial fusion events in a freshly isolated AVCM. Video corresponds to Fig. S3. Duration, 8.25 min; acquisition frequency, 0.33 Hz, at 7 fps.

Movie S8

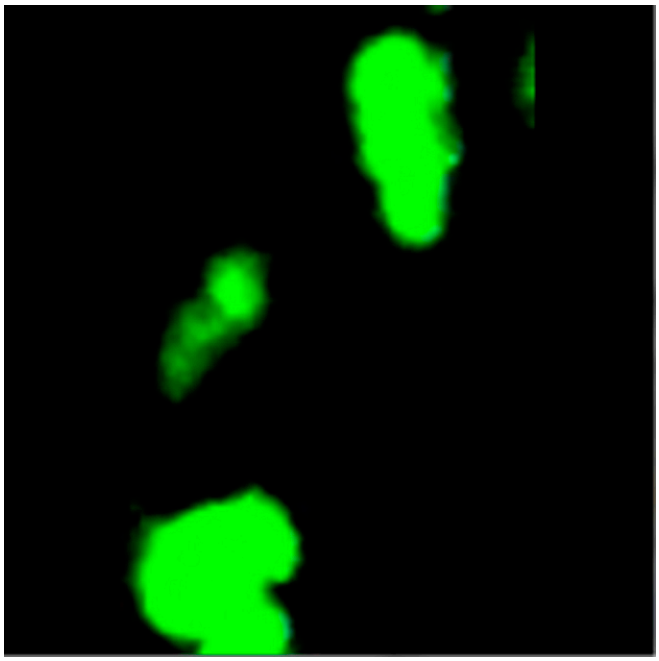

Movie S9. Motility and emerging nanotunnel in a freshly isolated AVCM. Video corresponds to Fig. S4, showing the motility of elongated mitochondria followed by a longitudinal fusion event. Duration, 8.25 min; acquisition frequency, 0.33 Hz, at 7 fps.

Movie S9